electronics

MDPI

Article

Fault-Resilient Coordinated Voltage Control of Electric–Hydrogen Hybrid Microgrids with Battery–Fuel Cell Synergy

Huichen Yu [1,2], Fulin Fan [1,2,*], Zhengyao Wang [1,2], Shihao Zhu [1,2], Jingran Zhang [3], Zhengjian Chen [3] and Kai Song [1,2,*]

[1] School of Electrical Engineering and Automation, Harbin Institute of Technology, Harbin 150001, China; 25s106179@stu.hit.edu.cn (H.Y.); 24b906052@stu.hit.edu.cn (Z.W.); 25b906043@stu.hit.edu.cn (S.Z.)
[2] Suzhou Research Institute, Harbin Institute of Technology, Suzhou 215104, China
[3] Shenzhen Energy Group Company Ltd., Shenzhen 518000, China; zhangjingran@sec.com.cn (J.Z.); chenzhengjian@sec.com.cn (Z.C.)
* Correspondence: fulin.fan@hit.edu.cn (F.F.); kaisong@hit.edu.cn (K.S.)

Abstract

Electric–hydrogen hybrid microgrids integrating distributed renewables with electrolysers can efficiently convert dispersed renewables into hydrogen, meeting local electricity demands. However, intermittent and uncertain renewables together with sudden load changes can cause severe bus voltage fluctuations and degrade power quality, especially in off-grid microgrids. Furthermore, the electrolyser's auxiliary units require stable AC power supply even during fault events, which most likely occur at AC–DC converters. To ensure stability during renewable/load fluctuations and converter faults, this paper proposes a fault-resilient coordinated voltage control scheme by combining PI with piecewise active disturbance rejection control to mitigate DC bus voltage fluctuations during transient disturbances and regulates AC-side fuel cells via control switching to stabilise AC voltage after the complete disconnection converter fault. The scheme is tested using a simulated kW-scale electric–hydrogen hybrid microgrid in various operating scenarios and compared with conventional methods that combine PI with PI or linear active disturbance rejection control. The simulation results show that the proposed control scheme improves DC bus voltage stability by 14% during transient renewable/load fluctuations via the incorporation of PADRC and enhance system resilience against AC–DC converter faults through the synergy of batteries and fuel cells, which construct the voltage (and frequency) of DC and AC buses, respectively.

Keywords: electric–hydrogen hybrid microgrid; piecewise active disturbance rejection control; voltage stabilisation; virtual synchronous generator; fault-resilient coordinated control

Check for updates

Academic Editor: Dorin Petreus

Received: 9 July 2026
Revised: 1 September 2026
Accepted: 2 September 2026
Published: 5 September 2026

Copyright: © 2026 by the authors. Licensee MDPI, Basel, Switzerland. This article is an open access article distributed under the terms and conditions of the Creative Commons Attribution (CC BY) license.

1. Introduction

The development of renewable-dominated power system serves as a crucial pathway toward the decarbonisation of the electricity and energy sectors. The increasing penetration of renewable generation and associated power electronic equipment introduce significant uncertainties and technical challenges that affect the efficiency of renewable energy usage. Power systems must possess sufficient flexibility to deal with real-time power imbalances induced by variable renewable generation [1–4]. To accommodate multi-timescale

fluctuations and surplus of renewables, long-duration energy storage and cross-sector coupling become essential. Hydrogen serves as a clean energy carrier capable of seasonal storage, offering a promising pathway to absorb surplus renewables and convert them into dispatchable energy. To further enhance cost efficiency within microgrids, excess wind and solar power can be utilised for water electrolysis, with the resulting high-purity hydrogen converted into liquid ammonia for easier storage and transport [5–7]. However, photovoltaic (PV) generation and electrolysers are intrinsically direct current (DC) devices, whereas the existing distribution grid and many loads operate on alternating current (AC). Frequent AC–DC–AC conversions not only degrade system efficiency, but also complicate flexible regulation. This drives an urgent need to develop diversified electric–hydrogen AC–DC hybrid microgrids that deeply integrate source–grid–load–storage flexible resources, minimising conversion losses while enhancing the controllability.

To ensure the green nature and stability of hydrogen production, electric–hydrogen coupled microgrids are generally required to have the capability of operating in islanded or off-grid modes. However, with the volatility and intermittency of renewable generation, the DC bus voltage can suffer from sharp fluctuations, significantly degrading the power quality of the DC link [8]. Numerous control methods have been proposed to accelerate the recovery speed and reduce voltage fluctuations. For instance, in the field of microgrid secondary control, ref. [9] proposed a model reference adaptive control (MRAC) scheme that employed reference models to represent desired voltage trajectories and adaptive algorithms to continuously update model parameters, achieving robust voltage recovery and precise active/reactive power sharing under uncertain operating conditions. In [10], cascaded PID controllers were tuned based on the integral of time-weighted absolute error criterion to achieve satisfactory voltage regulation performance. An adaptive control method tailored for DC microgrids was proposed in [11], achieving accurate current sharing and appropriate voltage regulation under varying load conditions. In [12], a novel segmented droop control strategy based on tolerance bands was introduced to mitigate voltage offset and oscillation issues. Additionally, to address the trade-off between voltage deviation and current sharing accuracy in conventional droop control where improving one would inevitably worsen the other, a family of distributed piecewise droop control strategies was proposed in [13] to simultaneously improve current sharing accuracy and voltage compensation. To address voltage instability in offshore microgrids caused by parameter mismatches and external disturbances, ref. [14] proposed an adaptive dual-loop gain ADRC (DGA-ADRC) method that integrates theoretical dual-loop gain matching with a soft actor–critic algorithm for adaptive parameter tuning.

Due to the lack of support from upstream grids, the fault-resilient control of islanded microgrids is also a key challenge. In addition to fault-resilient control within microgrids, sensor faults in electronically interfaced distributed energy resources (DERs) were considered in [15], where a fault-tolerant control method was developed by combining a sliding mode observer with an H-infinity output feedback controller so as to ensure microgrid resilience against erroneous measurements. To tackle actuator/sensor failures, a fault-tolerant state feedback observer-based controller was designed in [16], reducing the impact of noise and external disturbances on the fault estimation accuracy. An optimal fuzzy gain scheduling technique was leveraged in [17] to develop a fault-tolerant controller that mitigated the adverse effects of PV output loss faults. Ref. [18] proposed a coordinated control strategy for a wind–hydrogen–battery standalone microgrid, integrating a wind turbine generator with battery energy storage, electrolyser, and fuel cell to enhance power supply continuity and reliability under distribution line faults.

However, including the conventional nonlinear active disturbance rejection control (NLADRC), most existing voltage regulation schemes are relatively complex, posing chal-

lenges for practical implementation within hybrid microgrid projects, and lack effective suppression of large voltage fluctuations—specifically, those based on fixed-gain linear observers suffer from the contradiction between disturbance estimation speed and noise sensitivity, while other online identification-based approaches hinder real-time deployment. Furthermore, less attention has been paid to the control strategies that enable rapid microgrid reconfiguration and smooth switching under extreme fault conditions such as converter faults, which are the most common type of failure in microgrids [19]. Some studies have proposed recovery measures after converter faults from the perspectives of the converters themselves, though post-fault recovery processes rely entirely on hardware-level reconfiguration and lack the system-level topology reconfiguration or operational mode switching of microgrids, which could lead to an extended recovery time. To address these gaps, this paper proposes a DC bus voltage stabilisation strategy based on PI control combined with piecewise active disturbance rejection control (PADRC), integrated with a state-switching control mechanism designed for converter faults in the context of an electric–hydrogen AC–DC hybrid microgrid. The proposed approach forms a unified control framework that jointly considers dynamic performance and operational resilience. Specifically, PADRC is employed to observe and compensate for internal and external disturbances in real time, effectively mitigating voltage sags and swells caused by power fluctuations from DERs and load switching, thereby enhancing voltage regulation accuracy and dynamic response speed. Then, a multi-mode state-switching control scheme is developed to handle converter faults. Upon converter fault detection, the microgrid rapidly and seamlessly transitions to a pre-designed fault-tolerant operating mode, where electric–hydrogen hybrid energy storage units, DERs, and loads are coordinated to reconstruct the power balance of microgrid and maintain critical load supply, ensuring continuous and stable microgrid operation under converter fault conditions. The proposed method not only improves power quality during normal operation, but also significantly enhances system survivability and recovery capability under converter fault scenarios.

The rest of the paper is structured as follows: Section 2 introduces the modelling of the electric–hydrogen AC–DC hybrid microgrid; Section 3 describes the DC bus voltage regulation schemes under normal operation and control switching under converter fault conditions; Section 4 discusses simulation results of microgrid control under different operating scenarios; and conclusions and recommendations for future work are presented in Section 5.

2. Electric–Hydrogen AC–DC Hybrid Microgrid Modelling

2.1. Electric–Hydrogen AC–DC Hybrid Microgrid Scheme

The electric–hydrogen AC–DC hybrid microgrid simulated in this work comprises PV panels, a battery energy storage system (BESS), DC loads, and a proton exchange membrane electrolyser (PEMEL) on the DC side and fuel cells (FCs) and AC loads on the AC side, as shown in Figure 1. The PV panels are connected to the DC bus via boost converters and controlled by the maximum power point tracking (MPPT) based on the perturbation and observation (P&O) method to fully utilise solar energy [20]. The PEMEL is connected to the DC bus through a buck converter, and the BESS stabilises the DC bus voltage through a bidirectional buck–boost converter. Four FCs are cascaded by their corresponding DC–DC converters, with their aggregated outputs being sent to the AC bus through a DC–AC inverter.

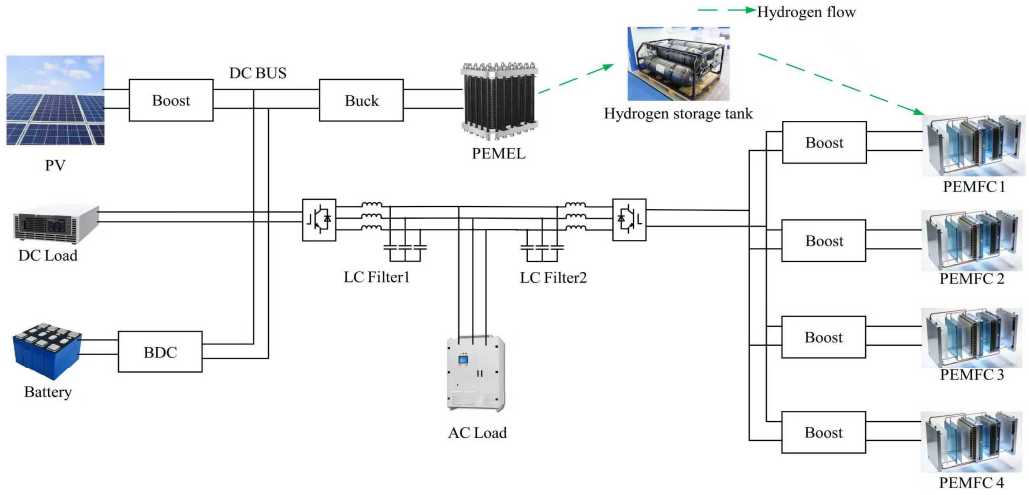

Figure 1. Schematic of an electric–hydrogen AC–DC hybrid microgrid.

2.2. PV Panel Model

A mathematical model of the PV panel is shown in Figure 2. It is mainly composed of a photogenerated current source, a diode, and parallel and series resistors. The output current of the photosensitive current source is denoted by I_{ph} (A); R_s and R_{sh} are the series resistance (Ω) and parallel resistance (Ω), respectively, indicating the internal loss of the PV array.

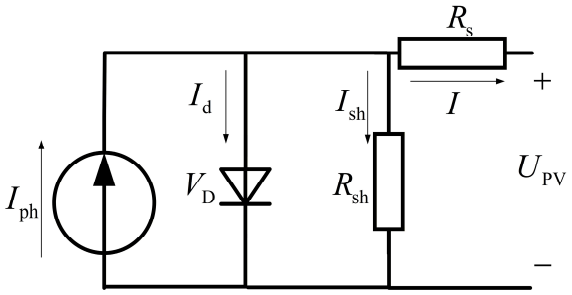

Figure 2. Mathematical model of a PV panel.

The V–A characteristic curve of the PV panel can be formulated by [21]

$$I = I_{ph} - I_0\left\{\exp\left[\frac{q(U_{PV} + IR_s)}{AKT}\right] - 1\right\} - \frac{U_{PV} + IR_s}{R_{sh}} \quad (1)$$

where I and U_{PV} are the output current (A) and voltage (V) of the PV panel, respectively; I_0 is the reverse saturation current (A); q denotes the electron charge (1.6×10^{-19} C); K is the Boltzmann's constant (1.38×10^{-23} J/K); T is the absolute temperature (K) of the PV panel; and A is the diode factor.

2.3. BESS Model

The BESS is modelled by the Thevenin equivalent circuit, which uses a parallel resistor–capacitor network to describe the voltage response dynamics during BESS operation, as shown in Figure 3 [22], where V_{OC} and R are the DC voltage source (V) and its internal resistance (Ω), respectively; and R_1 and C_1 are the polarisation resistor (Ω) and capacitor (F), respectively. To simplify the control-oriented design and focus on the dynamic response of the proposed voltage control schemes, the internal resistance R and polarisation resistance R_1 are assumed to be constant parameters [23].

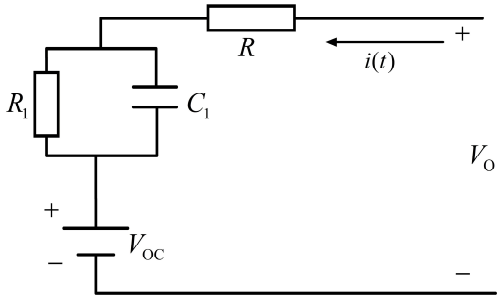

Figure 3. Thevenin model of the BESS.

According to the ampere-hour integration method, the state of charge (SOC) level of the BESS can be obtained by

$$\begin{cases} SOC(t+1) = SOC(t) - \frac{P_b \eta_c \Delta t}{C} \text{ for } P_b \leq 0 \\ SOC(t+1) = SOC(t) - \frac{P_b \Delta t}{\eta_d C} \text{ for } P_b > 0 \end{cases} \quad (2)$$

where $SOC(t)$ is the SOC of the BESS at time t; Δt is the time step (h); C is the battery capacity (kWh); η_c and η_d are the charging and discharging efficiencies of the BESS, respectively; and P_b is the power of the BESS (kW).

2.4. FC Model

An equivalent mathematical model of an FC is developed here based on its electrochemical characteristics. The actual terminal output voltage of a N-cell FC stack is lower than the open circuit voltage due to activation losses and ohmic losses inside the stack. This is formulated by [24]

$$\begin{cases} U_{fc} = E_{oc} - U_{act} - U_{ohm} \\ U_{act} = NA_{fc} \ln\left(\frac{i_{fc}}{i_0}\right) \frac{1}{sT_{delay}+1} \\ U_{ohm} = R_{ohm} i_{fc} \end{cases} \quad (3)$$

where U_{fc} and E_{oc} are the terminal output voltage and reversible open-circuit voltage of the FC stack (V), respectively; U_{act} or U_{ohm} is the activation or ohmic overvoltage (V), which represents the voltage loss caused by activation polarisation during electrochemical reactions or by the internal resistance R_{ohm} (Ω) of the membrane and electrodes, respectively; A_{fc} is the Tafel slope (V); i_{fc} is the FC output current (A); i_0 is the exchange current (A); and T_{delay} is the time constant (s).

2.5. Hydrogen Storage Tank Model

The pressure of the hydrogen storage tank p_s (Pa) and the corresponding state of hydrogen charge (SOHC) are formulated by [25]

$$p_s = \frac{R_s T_s}{V_s} \left(n_{s,0} + n_{aeH_2} - n_{fcH_2}\right) \quad (4)$$

$$SOHC = \frac{p_s}{p_{smax}} \times 100\% \quad (5)$$

where T_s, V_s, and p_{smax} are the temperature (K), internal volume (m^3), and maximum allowable pressure (Pa) of the hydrogen storage tank, respectively; R_s is the gas constant (J/(mol·K); $n_{s,0}$ is the initial molar amount (mol) of hydrogen storage; and n_{aeH_2} (mol) or n_{fcH_2} (mol) denotes the cumulative molar amount of hydrogen produced by the PEMEL or consumed by the FC from the initial moment to the current time step, respectively.

2.6. PEMEL Model

The operating voltage of a PEMEL consists of the thermodynamic reversible voltage required for the water electrolysis reaction, the activation overvoltage caused by electrochemical polarisation at anode and cathode, and the ohmic overvoltage induced by the internal resistance of the membrane and electrodes. The corresponding voltage model is formulated by [26,27]

$$\begin{cases} V_{\mathrm{el}} = E_{\mathrm{rev}} + V_{\mathrm{Act}} + V_{\mathrm{Ohm}} \\ E_{\mathrm{rev}} = E^{0}_{\mathrm{rev}} + \frac{R_{\mathrm{s}}}{2F} T_{\mathrm{el}} ln\left[\frac{P_{H_2}\sqrt{P_{O_2}}}{P_{H_2O}}\right] \\ V_{\mathrm{Act}} = \frac{R' T_{el}}{\alpha_{\mathrm{an}} F} sinh^{-1}\left(\frac{i'}{2j_{0,\mathrm{an}}}\right) + \frac{R' T_{el}}{\alpha_{\mathrm{cat}} F} sinh^{-1}\left(\frac{i'}{2j_{0,\mathrm{cat}}}\right) \\ V_{\mathrm{Ohm}} = R_{\mathrm{Ohm}} \cdot i' \\ R_{\mathrm{Ohm}} = \frac{\delta_m}{A_m \sigma_m} \end{cases} \tag{6}$$

where V_{el} is the operating voltage of the PEMEL (V); E_{rev}, V_{Act}, and V_{Ohm} are the thermodynamic reversible voltage, activation overvoltage, and ohmic overvoltage (all in V), respectively; E^{0}_{rev} is the standard reversible voltage in standard state (V); R_{s} is the universal gas constant (J/mol·K); T_{el} is the temperature (K) of PEMEL; F is the Faraday constant; $P_{\mathrm{H_2}}$, $P_{\mathrm{O_2}}$, or $P_{\mathrm{H_2O}}$ is the partial pressure (Pa) of hydrogen, oxygen, or water vapor, respectively; δ_{m}, σ_{m}, and A_{m} are the thickness (m), ionic conductivity (S/m), and effective area (m^2) of the membrane, respectively; i' is the operating current density ($\mathrm{A/m^2}$); R_{Ohm} is the internal ohmic resistance of PEMEL; α_{an} and α_{cat} are the charge transfer coefficients for the anode and cathode, respectively; and $j_{0,\mathrm{an}}$ and $j_{0,\mathrm{cat}}$ are the exchange current densities ($\mathrm{A/m^2}$) for the anode and cathode, respectively. It should be noted that the proposed model adopts a quasi-static assumption by treating the membrane ionic conductivity and internal parameters as constants. Since the coordinated voltage control and fault-tolerant schemes investigated in this paper operate on a millisecond-to-second timescale, the slower thermal and membrane water content dynamics have a negligible impact on the fast electrical transients. The integration of detailed water–thermal balance equations to improve long-term operational accuracy remains a promising direction for future work.

3. Coordinated Control of Electric–Hydrogen AC–DC Hybrid Microgrid

Since this paper focuses on real-time voltage regulation of the electric–hydrogen hybrid microgrid rather than energy management strategies, the rule-based energy management strategies proposed in previous work [28] are adopted here to simulate the power dispatch within the microgrid over a certain period, as shown in Figure 4. In the main, the operating mode of the microgrid is switched according to the SOC of the BESS and the SOHC of the hydrogen storage tank. The exceedance of PV outputs over AC and DC loads is mainly stored by the BESS and/or converted into hydrogen through the PEMEL, while insufficient PV generation is supplemented by the BESS, the FC, or both, depending on the relative levels of SOC and SOHC. In addition to the designed energy management strategies, this section describes the coordinated voltage control methods proposed for normal and fault conditions, including the DC–DC voltage regulation control for BESS, the DC–AC converter control inclusive of VSG control for master converter and PQ control for slave converter, and the switching control in the converter fault event.

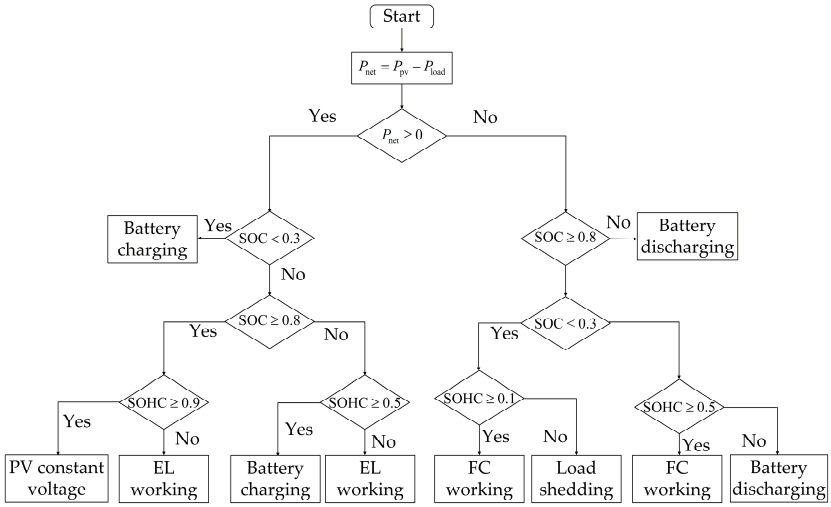

Figure 4. Flowchart of power management of an electric–hydrogen AC–DC microgrid.

3.1. DC–DC Voltage Regulation Control for the BESS

In the microgrid, the BESS is connected to the DC bus through a bidirectional buck–boost DC–DC converter, as shown in Figure 5. When the DC–DC converter operates in the boost mode, its state-space dynamic model can be formulated by (7):

$$\begin{cases} L\frac{di_{bat}}{dt} = U_{bat} + (g_2 - 1)U_{dc} \\ C\frac{dU_{dc}}{dt} = i_{dc} + (g_2 - 1)i_{bat} \end{cases} \tag{7}$$

where L and C are the filter inductance (H) and capacitance (F) of the converter, respectively; i_{bat} and U_{bat} are the current (A) and terminal voltage (V) of the batteries, respectively; U_{dc} and i_{dc} are the DC bus voltage (V) and output current (A) of the BESS, respectively; and $g_2 = 1$ or 0 indicates that the switching transistor S_2 is turned on or off, respectively. Similarly, when it operates in the buck mode, its state-space dynamic model can be formulated by

$$\begin{cases} L\frac{di_{bat}}{dt} = g_1U_{dc} - U_{bat} \\ C\frac{dU_{dc}}{dt} = i_{dc} - g_1i_{bat} \end{cases} \tag{8}$$

where $g_1 = 1$ or 0 indicates that the switching transistor S_1 is turned on or off, respectively. In this section, the control schemes of the widely used dual-loop PI, the PI with LADRC (PI + LADRC), and the proposed PI + PADRC are described. These will be applied to the BESS and tested separately to examine the advantages of the proposed PI + PADRC for the microgrid voltage stabilisation.

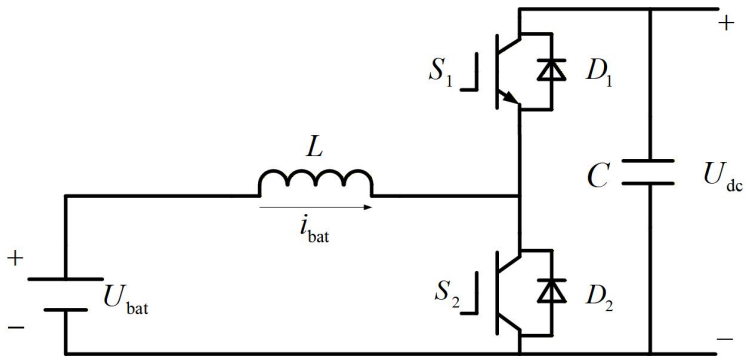

Figure 5. Basic model of a buck–boost DC–DC converter for the BESS.

3.1.1. PI + PI

For BESS-side bidirectional DC–DC converters, dual-loop PI control consisting of an outer voltage loop and an inner current loop is generally employed to stabilise the DC bus voltage and enhance the system stability, as shown in Figure 6. The outer voltage control loop detects the deviation of output voltage from the reference, which is processed by the voltage controller to generate a current reference signal as the input of the inner loop. Then, the inner current control loop collects the inductor current signal in real time and compares it with the current reference to produce the corresponding error signal. This error signal is processed by the current controller to export a duty cycle adjustment parameter. By performing pulse-width modulation with a carrier signal, a driving pulse sequence with adaptive duty cycle is generated to regulate the turn-on and turn-off sequences of power switching devices [29].

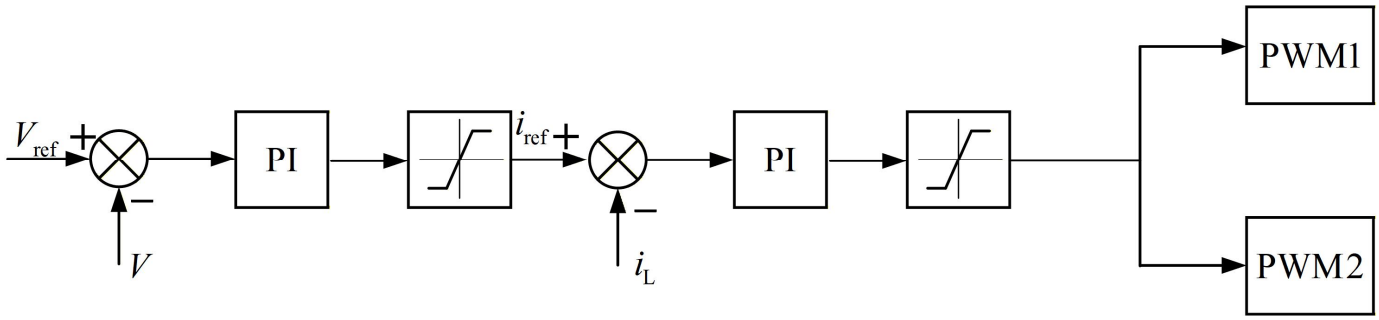

Figure 6. Dual-loop PI control scheme.

In the dual-loop control mechanism, the outer voltage loop is mainly responsible for the steady-state regulation of the output voltage, while the inner current loop tracks the dynamic variation of the inductor current in real time. However, when it is applied to a nonlinear, time-varying, and complex system, its control performance could be unsatisfactory. In addition, the cumbersome parameter tuning process makes it difficult to quickly find the optimal combination under different operating conditions. Meanwhile, its anti-disturbance effects are insufficient in strong disturbance environments. To that end, it cannot effectively suppress the influence of disturbances on system outputs.

3.1.2. PI + LADRC

To further improve the tracking accuracy of the inductor current in the inner current loop under steady-state conditions for bus voltage stabilisation, the current loop can be replaced with the first-order LADRC [30]. By controlling the inductor current to regulate the charging and discharging currents of BESS, fluctuation of DC bus voltage can be effectively suppressed, improving the rapid response and anti-interference ability of the system.

Using the first-order LADRC, the controlled objective of the inner current loop is the inductor current of the bidirectional DC–DC converter. Figure 7 shows the structure of the specific inner current-loop LADRC. The linear extended state observer (LESO) is used to track the actual value of the inductor current in real time and accurately estimate the total disturbance magnitude, providing a basis for disturbance compensation. Then, the linear state error feedback (LSEF) consisting of proportional control and disturbance compensation makes the inductor current quickly track the reference value through error feedback and disturbance cancellation.

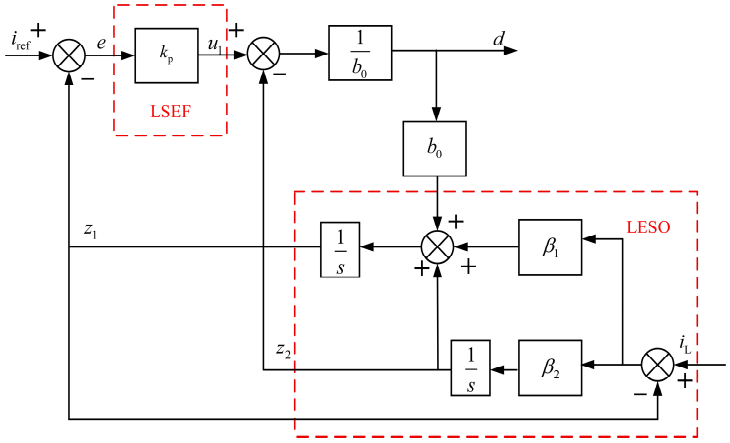

Figure 7. Structure of the inner current-loop LADRC.

Considering the equivalent series resistance of the inductor R_{L1}, the dynamic behavior of the bidirectional DC–DC converter in boost mode can be expressed as $L\dot{I}_L = V_{\text{bat}} - R_{\text{L}}I_{\text{L}} - (1-d)U_{\text{dc}}$. By defining the current attenuation coefficient $a = R_L/L$, the control gain $b = U_{\text{dc}}/L$, and grouping internal parameter perturbations with external disturbances into a total disturbance f, the inner-loop plant model is established as

$$\dot{I}_{\text{L}} = -aI_{\text{L}} + bd + f \tag{9}$$

where I_{L} is the inductor current, d is the duty cycle of switching transistor, and f is the total disturbance, inclusive of external and internal disturbances. External disturbances are mainly reflected in the uncertainties of PV output and DC bus voltage fluctuation caused by frequent load variations, while internal disturbances include the variation of internal parameters of the control system and the parameter perturbations of components inside the converter. The term a is the current attenuation coefficient dependent on the inherent characteristics of the converter, and b is the control gain coefficient.

By defining the state variables $x_1 = I_{\text{L}}$ and $x_2 = f - aI_{\text{L}}$, the control input $u = d$, and the compensation factor $b = U_{\text{dc}}/L$, the mathematical model of the LESO is formulated by

$$\begin{cases} \dot{z}_1 = z_2 - \beta_1(z_1 - I_{\text{L}}) + bd \\ \dot{z}_2 = -\beta_2(z_1 - I_{\text{L}}) \end{cases} \tag{10}$$

where z_1 and z_2 denote the estimated values of x_1 and x_2, respectively; and β_1 and β_2 are the observer gain coefficients. By employing the pole placement method, all the observer poles are set to $-\omega_0$, where ω_0 is the observer bandwidth. Then, the gain coefficients are formulated by

$$\begin{cases} \beta_1 = 2\omega_0 \\ \beta_2 = \omega_0^2 \end{cases} \tag{11}$$

Then, the resulting current tracking error relative to the reference, which is fed into the LSEF, is formulated by

$$e = i_{\text{ref}} - z_1 \tag{12}$$

To simplify the control structure and ensure the dynamic response speed, a proportional control is adopted to generate the basic control signal

$$u_1 = k_{\text{p}}e \tag{13}$$

where k_p is the proportional gain coefficient, determined by the controller bandwidth ω_c. Meanwhile, to facilitate parameter tuning, ω_0 and ω_c generally satisfy the following relationship in engineering [31]:

$$\omega_0 = (3 \sim 7)\omega_c \tag{14}$$

The selection of observer bandwidth ω_0 involves a trade-off among the disturbance estimation speed, noise sensitivity, and system stability. An excessively small ω_0 (e.g., below $3\omega_c$) could delay the disturbance estimation and result in sluggish dynamic responses, while an excessively large ω_0 (e.g., above $7\omega_c$) would amplify measurement noises, causing control signal chattering and increased steady-state ripples. Therefore, $\omega_0 = 5\omega_c$ is selected here as a compromise, achieving the balance between fast disturbance compensation and smooth control performance.

Combined with the disturbance estimation z_2 from LESO, a disturbance compensation mechanism is introduced in LSEF, with the duty cycle control signal being formulated by

$$d = \frac{u_1 - z_2}{b} \tag{15}$$

When the disturbance estimation is sufficiently accurate, the total disturbance is completely cancelled. The closed-loop transfer function of the LADRC is formulated as follows:

$$\frac{i_L(s)}{i_{ref}(s)} = \frac{k_p}{s + (k_p + a)} \tag{16}$$

Since $k_p > 0$ and the physical attenuation coefficient $a > 0$, the closed-loop pole is strictly located in the left-half plane, ensuring inherent system stability. Furthermore, by configuring the closed-loop pole to equal $-\omega_c$, the relationship between k_p and the controller bandwidth ω_c is explicitly given by $k_p = \omega_c - a$. In practical applications, a is exceptionally small, simplifying this to $k_p \approx \omega_c$. This first-order inertial element ensures the rapidity and accuracy of current tracking. It can be seen that a larger ω_c results in a wider control bandwidth, allowing the system to track higher-frequency disturbances. However, an excessively large ω_c will amplify the sampling noise of the current sensor, the switching noise of power electronic devices, and line harmonics. Therefore, during parameter tuning, ω_c should be increased gradually from a small value, while observing the variation of the bus voltage step by step.

3.1.3. PI + PADRC

In traditional LADRC, the LESO employs a fixed-gain error correction law, as formulated by (12), in which the product of β_1 or β_2 with the error determines the convergence rates. Due to the limited responsiveness of the linear correction term, the observer converges slowly when the system encounters large disturbances. To address this issue, this paper incorporates the PADRC by introducing nonlinear error terms into the ESO. First, to avoid symbol confusion with the tracking error defined in (12), the observer errors are redefined as $\varepsilon_1 = i_L - z_1$ and $\varepsilon_2 = x_2 - z_2$.

To ensure correct damping polarity while providing differentiated acceleration for the state and disturbance channels, a nonlinear function is introduced. Unlike conventional pure square terms that lose sign information, the form of $\varepsilon_1|\varepsilon_1|$ is utilised to maintain correct polarity. To balance convergence speed and noise sensitivity, the nonlinear gains are configured with a proportional relationship, defined as $k_1 = 10k_2$. To suppress steady-state chattering induced by measurement noise, a threshold mechanism is applied exclusively to the state tracking channel. The ESO of the PADRC is formulated as a piecewise function:

$$\begin{cases} \dot{z}_1 = z_2 + \beta_1 \varepsilon_1 + k_1 \cdot \Psi(\varepsilon_1) + bd \\ \dot{z}_2 = \beta_2 \varepsilon_1 + k_2 \cdot \varepsilon_1 |\varepsilon_1| \end{cases} \tag{17}$$

where $\Psi(\varepsilon_1) = \begin{cases} \varepsilon_1 |\varepsilon_1| \ |\varepsilon_1| > \delta \\ 0 \ |\varepsilon_1| < \delta \end{cases}$ and $\beta_1 = 2\omega_o$ and $\beta_2 = \omega_o^2$ are the linear observer gains; k_1 and k_2 are the nonlinear gain coefficients; and δ is the threshold parameter. With large errors, the term $k_1 \varepsilon_1 |\varepsilon_1|$ strongly accelerates state estimation, while $k_2 \varepsilon_1 |\varepsilon_1|$ smoothly accelerates disturbance estimation. With small errors, the state channel reverts to linear correction to prevent noise amplification, whereas the disturbance channel retains $k_2 \varepsilon_1 |\varepsilon_1|$ to continuously enhance estimation precision.

To analyse the frequency domain characteristics with large disturbances, a frozen-error linearisation approach is adopted for the region $|\varepsilon_1| > \delta$. By treating the time-varying term $|\varepsilon_1|$ as an instantaneous equivalent gain $G_{eq} = |\varepsilon_1|$, the nonlinear ESO is approximated as a linear time-varying system with augmented gains:

$$\begin{cases} \dot{z}_1 = z_2 + (\beta_1 + k_1 G_{eq}) \varepsilon_1 + bd \\ \dot{z}_2 = (\beta_2 + k_2 G_{eq}) \varepsilon_1 \end{cases} \tag{18}$$

Applying the Laplace transform to the linearised ESO, the disturbance observation transfer function is derived as

$$G_{z_2}(s) = \frac{Z_2(s)}{I_L(s)} = \frac{(\beta_2 + k_2 G_{eq}) s}{s^2 + (\beta_1 + k_1 G_{eq}) s + (\beta_2 + k_2 G_{eq})} \tag{19}$$

Compared to the fixed bandwidth of the conventional LADRC, the equivalent bandwidth of the PADRC increases automatically under large disturbances. Furthermore, its equivalent damping ratio transitions from $\zeta_{linear} = \frac{\omega_0}{\sqrt{\omega_0{}^2 + k_2 G_{eq}}}$ in the small-error region to ζ_{PADRC} in the large-error region:

$$\zeta_{PADRC} = \frac{\beta_1 + k_1 G_{eq}}{2\sqrt{\beta_2 + k_2 G_{eq}}} \tag{20}$$

Given the configuration of $k_1 = 10k_2$, $\zeta_{PADRC} > 1$ can readily imply an overdamped response with two strictly negative real poles, hence asymptotic stability. The PADRC exhibits uniform ultimate boundedness across all operating conditions: the equivalent bandwidth adaptively increases with large errors for fast convergence while reverting to the linear low-gain mode with small errors to suppress noise amplification.

To prevent the high-frequency numerical chattering that inevitably arises at the switching boundary due to the zero-order hold (ZOH) effect when the PADRC is implemented on a digital signal processor, the hard-switching function in (17) is replaced by a hysteresis-based smooth transition. The modified error correction is defined as

$$\Psi(\varepsilon_1) = \begin{cases} \varepsilon_1 |\varepsilon_1| \ |\varepsilon_1| > \delta + \epsilon \\ \frac{|\varepsilon_1| - \delta + \epsilon}{2\epsilon} \varepsilon_1 |\varepsilon_1| \ \delta - \epsilon \le |\varepsilon_1| \le \delta + \epsilon \\ 0 \ |\varepsilon_1| < \delta - \epsilon \end{cases}$$

where ϵ is the hysteresis bandwidth, selected as $\epsilon = 0.1\delta$. This linear interpolation removes the abrupt discontinuity at $|\varepsilon_1| = \delta$, ensuring that the control signal does not toggle between two distinct modes with measurement noise or discrete sampling, thereby eliminating the root cause of ZOH-induced numerical chattering.

Assuming the derivative of the total disturbance is bounded ($|\dot{x}_2| \le H$), the local asymptotic stability (LAS) of both subsystems is evaluated by linearising around the origin.

For the small-error subsystem, the Jacobian matrix yields the characteristic equation $\lambda^2 + \beta_1\lambda + \beta_2 = 0$. For the large-error subsystem, it yields $\lambda^2 + (\beta_1 + k_1 G_{eq})\lambda + (\beta_2 + k_2 G_{eq}) = 0$. Since the linear observer gains β_1 and β_2 are strictly positive, both characteristic equations perfectly satisfy the Hurwitz criterion. This confirms local asymptotic stability near the origin for each subsystem individually. However, because linearisation is only valid in a sufficiently small neighbourhood of the origin, it does not by itself guarantee global behaviour during large transients where $|\varepsilon_1|$ is not infinitesimal.

To establish global asymptotic stability (GAS), we construct an explicit piecewise quadratic Lyapunov function $V(\varepsilon) = \varepsilon^T P \varepsilon$, with $\varepsilon = [\varepsilon_1, \varepsilon_2]^T$. For the small-error subsystem, choosing $P = \frac{1}{2}\begin{bmatrix} \beta_1^2 + \beta_2 & \beta_2 \\ \beta_1 & 2 \end{bmatrix}$ yields $\dot{V} = -\varepsilon_1^2 - \beta_2\varepsilon_2^2 < 0$, which is strictly negative definite. For the large-error subsystem, the system matrix is $A_{large} = \begin{bmatrix} -(\beta_1 + k_1 G) & 1 \\ -(\beta_2 + k_2 G) & 0 \end{bmatrix}$, where $G = \mid \varepsilon_1 \mid^{-1} > 0$. Since A_{large} is Hurwitz for all $G > 0$ and the parameter G is bounded, one can select a parameter-dependent $P(G)$ such that $A_{large}^T P(G) + P(G) A_{large} = -I$, guaranteeing $\dot{V} = - \parallel \varepsilon \parallel^2 < 0$ uniformly.

Regarding the switching boundary at $\mid \varepsilon_1 \mid = \delta$, the transversality condition is analysed. The difference in the state derivatives between the two subsystems is $\Delta\dot{\varepsilon}_1 = -k_1\delta^2 \mathrm{sgn}(\varepsilon_1)$. Using the explicitly constructed V above, the difference of the Lyapunov derivatives across the boundary is derived as $\Delta\dot{V} = -(\beta_1 k_1 + k_1^2 G)\delta^2 < 0$ for some bounded $G > 0$. This negative jump in $\dot{V}$ rigorously precludes any sliding motion or chattering along the switching surface. Consequently, the cross-boundary condition guarantees that the trajectory inevitably enters the small-error region, where exponential convergence to the origin follows. Therefore, the switched system is globally asymptotically stable.

Applying the forward Euler method with a sampling period T_s to the piecewise ESO in (17), the discrete-time model of the PADRC is formulated as

$$\begin{cases} z_1(k+1) = z_1(k) + T_s[z_2(k) + \beta_1\varepsilon_1(k) + k_1 \cdot \Psi(\varepsilon_1(k)) + bd(k)] \\ z_2(k+1) = z_2(k) + T_s[\beta_2\varepsilon_1(k) + k_2 \cdot \varepsilon_1(k)|\varepsilon_1(k)|] \end{cases} \tag{21}$$

In the discrete-time domain, a hidden limit cycle can only occur if the trajectory skips over the boundary without the nonlinear term $k_1\Psi(\varepsilon_1)$ being activated. To prevent this, the state must not jump across the entire width of the threshold δ within one sampling step. The necessary condition for the existence of a restoring action at the boundary is $T_s|\dot{\varepsilon_1}|_{max} < \delta$. The maximum rate of change of the observer error is bounded by the nonlinear correction term, which is approximately $k_1\delta$ when $|\varepsilon_1| \approx \delta$. This leads to the critical sampling condition $T_s < \frac{1}{k_1}$.

To rigorously evaluate the parameter sensitivity of the proposed PADRC, an analytical sensitivity analysis is conducted based on the equivalent frequency domain characteristics. Due to the piecewise nature of the switching function $\Psi(\varepsilon_1)$ in (17), traditional gradient-based sensitivity is mathematically ill-defined at the boundary $|\varepsilon_1| = \delta$. Therefore, the sensitivity is evaluated by analysing how the parameters k_1, k_2, and δ map to the variations of the equivalent observer bandwidth ω_{eq} and equivalent damping ratio ζ_{eq} across the two distinct regions.

For sensitivity to k_2, in both regions, the equivalent bandwidth $\omega_{eq} = \sqrt{\omega_0{}^2 + k_2|\varepsilon_1|}$ is identical. Its partial derivative with respect to k_2 is

$$\frac{\partial\omega_{eq}}{\partial k_2} = \frac{|\varepsilon_1|}{2\sqrt{\omega_0^2 + k_2|\varepsilon_1|}} \geq 0 \tag{22}$$

This proves that ω_{eq} is strictly monotonically increasing with k_2, accelerating disturbance estimation. However, the sensitivity $\frac{\partial \omega_{eq}}{\partial k_2}$ decreases as k_2 increases, explaining the diminishing marginal return of continuously increasing k_2.

Furthermore, observing the equivalent damping ratio, an increase in k_2 enlarges the denominator in both regions, which decreases ζ_{eq}. In the small-error region, a decreased ζ_{linear} implies a tendency towards underdamped oscillations. This analytically restricts the upper limit of k_2 to prevent steady-state tracking ripples.

For sensitivity to k_1, in the large-error region, the partial derivative is

$$\frac{\partial \zeta_{eq}}{\partial k_1} = \frac{|\varepsilon_1|}{2\sqrt{\omega_0^2 + k_2|\varepsilon_1|}} \geq 0 \tag{23}$$

The system gains positive sensitivity to k_1. Given the configuration $k_1 = 10k_2$, this positive sensitivity rapidly forces $\zeta_{PADRC} > 1$, transitioning the observer into an overdamped state to suppress state estimation overshoot during severe disturbances.

For sensitivity to δ, the threshold δ acts as the decision boundary determining which set of dynamic equations governs the system. Its sensitivity is evaluated by analysing the structural changes at the boundaries:

An excessively small δ keeps the nonlinear term $\Psi(\varepsilon_1)$ continuously activated. This forces the system to remain in the overdamped state even during steady-state operation, which directly causes the undesirable amplification of sensor noise chattering.

An excessively large δ prevents activation of the nonlinear term during large transient fluctuations. This forces the system to permanently operate in the small-error mode, losing its overshoot suppression capability.

Based on the ESO structure of the PADRC given in (17), the measurement noise propagation path is rigorously derived to evaluate its impact on the control signal. The actual inductor current is contaminated by sensor noise as $i_L^{meas} = i_L + n$. By adopting the frozen-error linearisation $G_{eq} = |\varepsilon_1|$ and applying the Laplace transform under zero initial conditions, the transfer functions from the measurement noise $N(s)$ to the duty cycle $D(s)$ are obtained for distinct operating regions. In the small-error region, the transfer function is formulated by

$$G_{n\to d}^{small}(s) = -\frac{1}{b}\frac{[k_p\beta_1 + (\beta_2 + k_2G_{eq})]s + k_p(\beta_2 + k_2G_{eq})}{s^2 + \beta_1 s + (\beta_2 + k_2G_{eq})} \tag{24}$$

In the large-error region, the transfer function is formulated by

$$G_{n\to d}^{large}(s) = -\frac{1}{b}\frac{[k_p(\beta_1 + k_1G_{eq}) + (\beta_2 + k_2G_{eq})]s + k_p(\beta_2 + k_2G_{eq})}{s^2 + (\beta_1 + k_1G_{eq})s + (\beta_2 + k_2G_{eq})} \tag{25}$$

For comparison, the conventional LADRC is formulated by

$$G_{n\to d}^{LADRC}(s) = -\frac{1}{b}\frac{(k_p\beta_1 + \beta_2)s + k_p\beta_2}{s^2 + \beta_1 s + \beta_2} \tag{26}$$

Figure 8 shows the frequency response magnitudes of these three transfer functions. Because β_2 is excessively large compared with k_2G_{eq}, during small disturbances PADRC and LADRC exhibit virtually no difference in noise rejection. During large disturbances, however, the low-frequency magnitude of PADRC is significantly lower than that of the two controllers during small disturbances. The activation of the nonlinear gain in the state channel further increases the equivalent bandwidth and damping ratio, driving the closed-loop poles deeper into the left half-plane. At high frequencies, the extra zeros introduced

raise the numerator order, causing a slight rebound in magnitude, yet the noise rejection remains satisfactory.

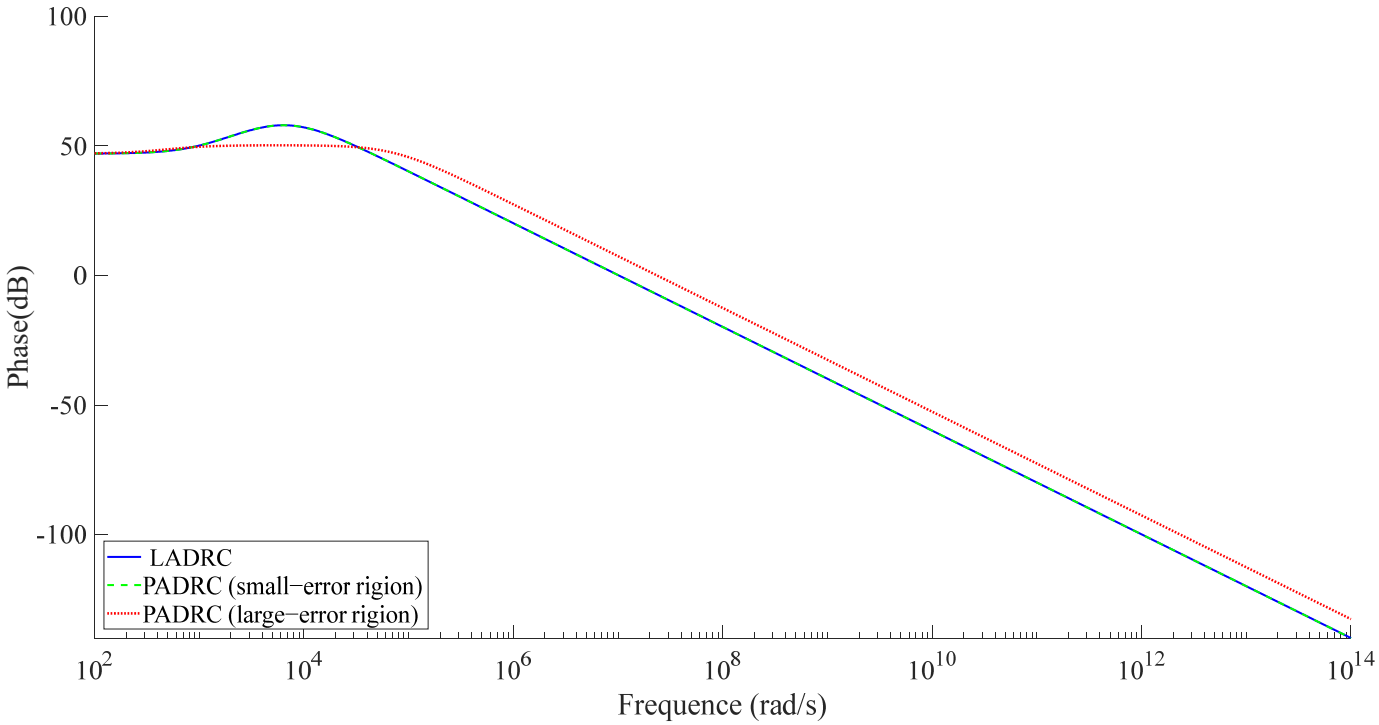

Figure 8. Frequency response magnitudes of three transfer functions.

3.2. DC–AC Converter Control

3.2.1. VSG Control for Master DC–AC Converter

VSG control plays an important role in the AC side of grid-forming systems [32]. By simulating the dynamic characteristics of synchronous generators, it enhances the inertial response and frequency disturbance rejection capability of the system. The VSG control includes active power frequency (P-f) control, reactive power voltage (Q-V) control, and virtual impedance control.

The VSG control algorithm is usually designed based on the swing equation of synchronous generators. The rotor motion is formulated by

$$J\frac{d\omega}{dt} = T_{\mathrm{m}} - T_{\mathrm{e}} - D(\omega - \omega_{\mathrm{n}}) \tag{27}$$

where J is the virtual moment of inertia (kg·m^2); ω and ω_{n} are the actual angular velocity and its rotor reference (rad/s), respectively; T_{m} is the mechanical torque provided by the prime mover (N·m); T_{e} is the output electromagnetic torque of generator (N·m); and D is the damping coefficient (kg·m^2/s). Similar to the mathematical model of synchronous generators, the P-f relationship is formulated by

$$J\frac{d\omega}{dt} = \frac{P_{\mathrm{m}}}{\omega_{\mathrm{n}}} - \frac{P}{\omega_{\mathrm{n}}} - D(\omega - \omega_n) \tag{28}$$

where P_{m} and P represent the mechanical and electromagnetic power (W), respectively. According to Equation (27), the virtual inertia coefficient and damping coefficient in VSG control mitigate the transient changes in microgrid frequency caused by active power variations, thereby ensuring the frequency stability of microgrid. In addition, a P-f droop

control loop is incorporated into the control strategy to simulate the primary frequency regulation characteristics of synchronous generators. This is formulated by

$$P_{\mathrm{m}} = P_{\mathrm{set}} - K_{\mathrm{f}}(\omega - \omega_{\mathrm{n}}) \tag{29}$$

where P_{set} is the active power reference value (W), and K_{f} is the active power frequency droop coefficient.

In addition to P-f regulation, the VSG can simulate the excitation system of conventional generators to achieve voltage support in power system. In other words, the terminal voltage and reactive power can be regulated by adjusting the virtual electromotive force. The reactive power regulation part is formulated by

$$\Delta E = n(Q_0 - Q) \tag{30}$$

where n is the reactive power droop coefficient; and ΔE is the change in the virtual electromotive force driven by the reactive power imbalance $(Q_0 - Q)$. Then, the reactive power voltage control of equation is formulated by

$$n(Q_0 - Q) = E - E_0 \tag{31}$$

where E_0 and E are the rated reference and actual output voltage, respectively.

To simulate the electrical characteristics of the synchronous generator stator, an electromagnetic field equation is introduced to reflect the relationship between the internal electromotive force and output voltage of the VSG, thereby forming the virtual impedance control. This is formulated by

$$e_{\mathrm{abc}} = R_{\mathrm{s}} i_{\mathrm{abc}} + L_{\mathrm{s}} \frac{di_{\mathrm{abc}}}{dt} + u_{\mathrm{abc}} \tag{32}$$

where e_{abc}, u_{abc}, and i_{abc} represent the internal electromotive force (V), output voltage (V), and current (A) of the VSG, respectively; and R_{s} and L_{s} denote the virtual synchronous resistance (Ω) and reactance (H), respectively.

After obtaining the reference voltage, voltage current double closed-loop control is adopted to achieve stable control of system. The specific process of VSG control of the master converter is shown in Figure 9. In this work, the virtual inertia and damping coefficients are set to fixed values, which are tuned to provide adequate frequency support for the millisecond-to-second timescale transients considered in the fault scenarios. The incorporation of an adaptive VSG strategy is identified as a direction for future work.

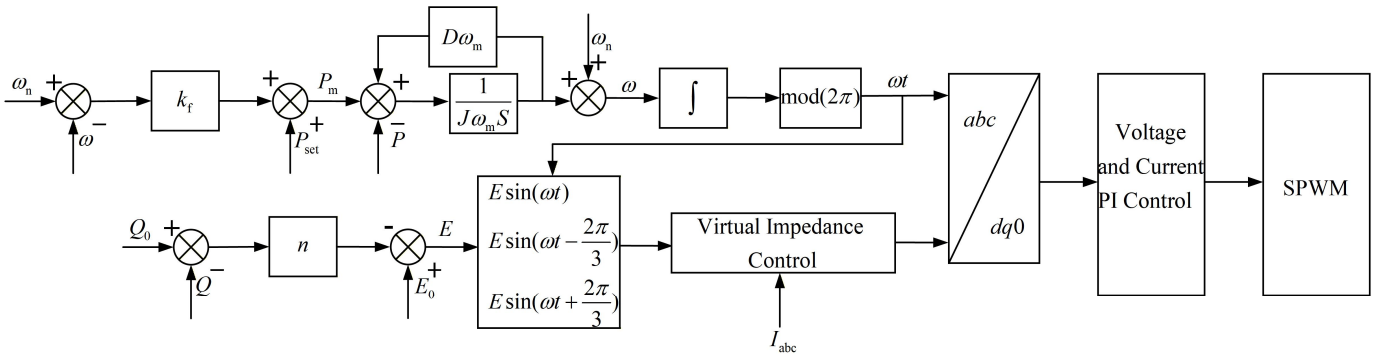

Figure 9. Block diagram of the master converter under VSG control.

3.2.2. PQ Control for Slave DC–AC Converter

The DC–AC converter of FCs acts as a slave converter adopting PQ control. When the microgrid operates in an islanded mode, the reference values of frequency and voltage for the slave converter are determined by those of the master converter. In actual operation, active and reactive power references (denoted by P_{ref} in W and Q_{ref} in Var) of the slave converter are tracked by adjusting the active and reactive currents. Specifically, the power calculation is based on the amplitude-invariant Park transformation where the d-axis is aligned with the grid voltage vector. Using this convention, the q-axis component of the voltage is zero, and the power equations are formulated as follows:

$$\begin{cases} P_{\text{ref}} = \frac{3}{2} V_{\text{d}} I_{\text{dref}} \\ Q_{\text{ref}} = -\frac{3}{2} V_{\text{d}} I_{\text{qref}} \end{cases} \tag{33}$$

where V_{d} is the voltage transformation value (V) at the interface between the master and slave converters; and I_{dref} and I_{qref} are the d- and q-axis reference currents (A) of the slave converter, respectively. These currents are fed into the current controller in the inner loop.

3.3. Control Switching After Converter Fault

To address converter faults, a fault detection device is introduced onto the DC bus. Specifically, the physical fault considered in this work is defined as a severe complete disconnection that abruptly drops the DC input voltage of the converter to zero. When this occurs, a comparator evaluates the DC voltage and activates an RS latch (with the R-port grounded). This latch permanently locks the switching command, driving a hardware switch module to instantaneously isolate the faulty converter and disable its gate signals. To ensure robustness against transient noise, a detection persistence time of 1 ms is incorporated into the detection logic, effectively serving as a hysteresis mechanism that prevents false triggering. Only when the zero-voltage condition persists continuously for at least 1 ms is the fault confirmed. Simultaneously, the control mode of the slave converter transitions from PQ to V-f. Critically, to avoid the physical reactant starvation issue of FCs under an instantaneous 20 kW step load, a power ramp rate limiter (20 kW/s) is inserted right after the power reference generation in the V-f controller, which practically emulates the slow mechanical inertia and delay of the air compressor. This approach immediately isolates non-critical loads that are inconsistent with the current FC output when faults occur and then sequentially restore these loads as FC power ramps up. Importantly, to achieve seamless initialisation of control and modulation states, the scheme directly inherits the real-time pre-fault AC bus voltage and frequency as initial targets. Furthermore, the integral states of the PI controllers in both the voltage outer loop and the current inner loop are initialised with their pre-switching steady-state output values. Concurrently, the PQ and V-f controllers share the same triangular carrier, and the switch module selects the active modulation signal without interrupting the carrier. Since the carrier phase is never reset or altered during the transfer, the resulting PWM pulses remain inherently continuous and glitch-free. Meanwhile, hot standby FCs are automatically connected to compensate for any electricity supply shortage. The coordinated operation of fault isolation, control mode switch, and redundant FC activation ensures that FCs and the BESS maintain a stable power supply to both AC and DC loads throughout the fault event. Once the converter fault is cleared and normal operating conditions are restored, the latch releases, and the controller returns to its standard regulation mode. The fault-resilient control switching scheme for the slave converter in the specific converter fault event is shown in Figure 10.

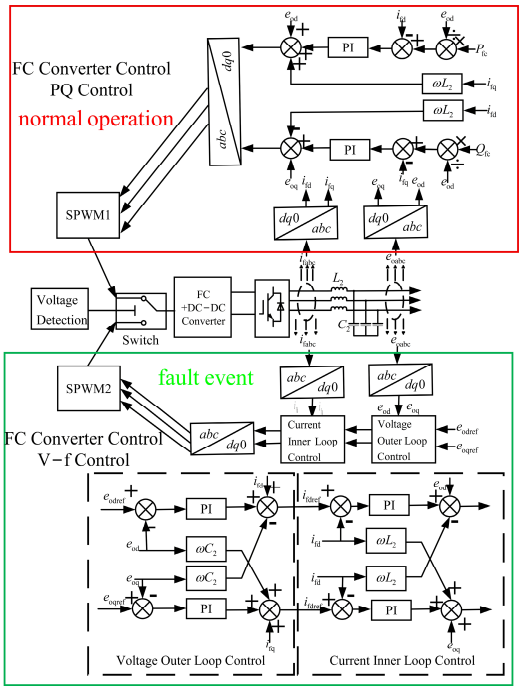

Figure 10. Scheme of fault-resilient control switching for the slave converter.

4. Results and Discussions

The PI + PADRC-based coordinated voltage control scheme proposed here is tested in the context of the isolated electric–hydrogen AC–DC hybrid microgrid, as shown in Figure 1, under various operating conditions and compared with the PI + PI− or PI + LADRC-based control scheme to validate the advantages of PI + PADRC in voltage stabilisation. In addition, the effectiveness of the fault-resilient control switching for the slave converter is assessed in the context of a fault occurrence on the converter, showcasing the synergy of FCs and the BESS for voltage stability and secure electricity supply on both the DC and AC sides during fault events. Modelling of the electric–hydrogen microgrid along with the proposed control method is accomplished in Matlab/Simulink R2022b. The simulation employs an ode14x solver (for further details of simulation modules, the reader is referred to Supplementary Materials). The technical parameters of the microgrid and its components are tabulated in Table 1 [33]. The technical parameters of the control schemes are tabulated in Table 2. The equivalent design conditions are guaranteed by subjecting all three schemes to identical outer-loop voltage control and physical actuator saturation limits, enabling a fair comparison between the conventional PI at its safe dynamic limit and the ADRC methods at their elevated architectural limits. The observer bandwidth ω_0 is bounded by the switching frequency f_s ($\frac{\pi}{5} f_s \leq \omega_0 \leq \frac{2\pi}{5} f_s$). The proportional gain of the PI controller is determined by the closed-loop bandwidth ($\omega_{c,PI}$) limit under the digital delay and the phase margin requirement, according to pole-zero cancellation ($K_p = L\omega_{c,PI}$). The controller parameters are strictly designed to avoid exciting the physical resonant frequency of the LC filter, given by $\omega_{LC} = 1\frac{1}{\sqrt{LC}} = 3162$ rad/s. For the LADRC and PADRC, the controller bandwidth is selected as $\omega_c = 1300$ rad/s, which rigorously satisfies the separation principle constraint $\omega_c \leq \omega_{LC}/2$, ensuring sufficient attenuation of LC resonance.

Table 1. Technical parameters of the electric–hydrogen AC–DC microgrid and related components.

Parameter		Value
DC bus voltage reference		750 V
AC bus voltage reference		380 V
Rated frequency		50 Hz
Virtual inertia		0.5 kg·m^2
Damping coefficient		4000 N·m·s/rad
LC Filter1 inductor		2 mH
LC Filter1 capacitor		0.01 mF
LC Filter2 inductor		2 mH
LC Filter2 capacitor		0.02 mF
Line equivalent resistor		5 mΩ
Line equivalent inductor		0.036 mH
PV generator	Maximum power	170 kW
	Voltage at MPP	41.32 V × 12
	Current at MPP	13.19 A × 26
Fuel cells	Rated power (four cascaded FC stacks)	200 kW
	Rated voltage	625 V
PEM electrolyser	Rated power	49 kW
Hydrogen storage tank	Maximum pressure	70 MPa
BESS	Rated capacity	400 Ah
	Rated voltage	500 V
Discrete time		1 μs
Switching frequency		10,000 Hz
Measurement filter		$\frac{30\pi}{s+30\pi}$
BESS-side DC–DC converter inductance		1 mH
BESS-side DC–DC converter capacitance		10 mF

Table 2. Technical parameters of the three control schemes.

Scheme	Parameter	Value
All	Voltage Loop K_p	120 A/V
	Voltage Loop K_i	1.2 A/(V·s)
PI + PI	Current Loop K_p	0.1/A
	Current Loop K_i	10/(A·s)
PI + ADRC	b	$\frac{200}{3}$ A/s
	ω_0	6500 rad/s
	ω_c	1300 rad/s
PI + PADRC	δ	1 A
	k_1	60/(A·s)
	k_2	6/(A·s)

4.1. DC Bus Voltage Regulation

To verify the superiority of the proposed PI + PADRC control scheme over the PI + PI and PI + LADRC schemes, two particular operating scenarios with different disturbances

are designed to simulate the voltage regulation of the three control schemes and evaluate their performance in terms of two key indicators, i.e., the transient fluctuation amplitude of DC bus voltage and the transient recovery time of inductor current.

4.1.1. Scenario I with Low SOC and High SOHC

Scenario I starts with initial conditions of SOC = 10% and SOHC = 90%, in which case the surplus or shortage of PV power outputs relative to the total load would be stored by the BESS or met by the FC, respectively. Table 3 lists the designed variations in PV outputs, DC loads, and AC loads over a 2 s interval.

Table 3. Variations of PV outputs, DC loads, and AC loads in Scenario I.

Power \ Time	Stage I 0–0.25 s	Stage II 0.25–0.3 s	Stage III 0.3–0.5 s	Stage IV 0.5–1 s	Stage V 1–1.5 s	Stage VI 1.5–2 s
PV Power (kW)	170	170	102.5	102.5	170	102.5
DC Load (kW)	12	8	8	8	8	8
AC Load (kW)	100	100	100	120	120	120

The dynamics of PV outputs, BESS export, FC export, PEMEL loads, and total microgrid loads using the three control schemes in Scenario I are shown in Figure 11a–c. Under the challenging conditions of Scenario I with low BESS SOC and high SOHC, all three control schemes ensure the voltage stability of the microgrid. However, compared with the PI + PI scheme, the PI + LADRC and PI + PADRC schemes result in relatively more stable BESS responses in the cases of the disturbances at 0.5 s and 1.5 s. This smoother transient behaviour mitigates the risk of overcharging and over-discharging of the BESS.

The corresponding dynamics of DC bus voltage under the three control schemes in Scenario I are shown in Figure 12a–c. According to Table 3, the events at 0.25 s, 0.3 s, 1.0 s, and 1.5 s are classified as small disturbances (smoothly absorbed by the BESS on the DC side), whereas the event at 0.5 s is classified as a large disturbance (AC load step coupled through the master converter). It is worth noting that the slight high-frequency fluctuations observed in the steady state are inherent switching ripples common to all control schemes, which do not affect the overall stability.

Under the small disturbance conditions (e.g., at 0.3 s and 1.5 s), the PI + PI scheme exhibits severe asymmetric overshoots, with deviations reaching −4.5 V/+7.7 V and −5.6 V/+8.9 V, respectively. In contrast, the PI + PADRC effectively restricts these fluctuations to −3.1 V/+1.7 V and −3.3 V/+3.7 V, successfully eliminating the positive overshoots observed under PI + PI, as tabulated in Table 4. Furthermore, across all small-disturbance events, PI + PADRC and PI + LADRC exhibit nearly identical deviations, illustrating that the proposed threshold mechanism prevents unnecessary activation of nonlinear correction with small errors.

Table 4. DC bus voltage fluctuation ranges in Scenario I using the three control schemes.

Disturbance Time (s)	Control Scheme	Bus Voltage Fluctuation Range (V)
0.3	PI + PI	745.5~757.7
	PI + LADRC	746.9~751.8
	PI + PADRC	746.9–751.7
0.5	PI + PI	742.6~762.6
	PI + LADRC	741.4~757.8
	PI + PADRC	742.6–756.7

Table 4. *Cont.*

Disturbance Time (s)	Control Scheme	Bus Voltage Fluctuation Range (V)
1.0	PI + PI	749.0~754.6
	PI + LADRC	748.7~752.9
	PI + PADRC	748.8–753.0
1.5	PI + PI	744.4~758.9
	PI + LADRC	746.3~753.3
	PI + PADRC	746.7–753.7

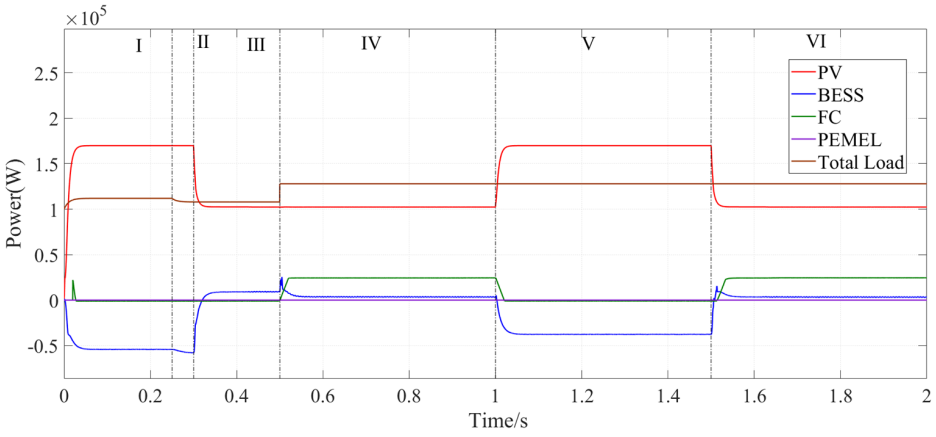

(**a**) PI + PI-based

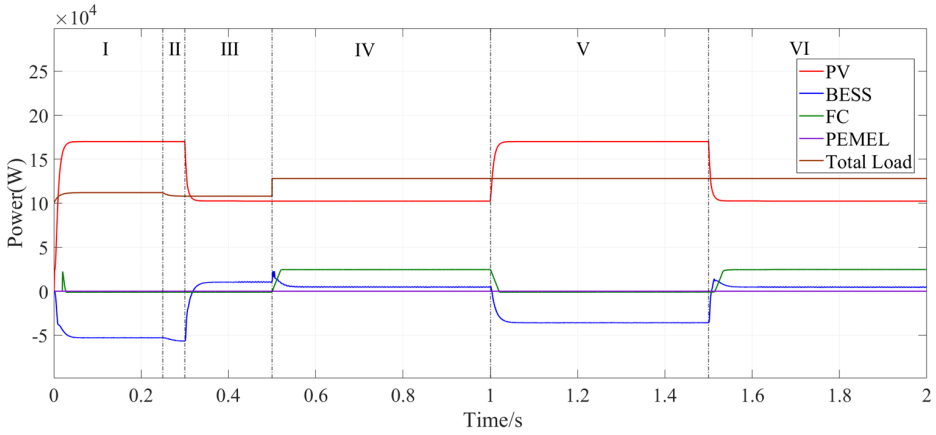

(**b**) PI + LADRC-based

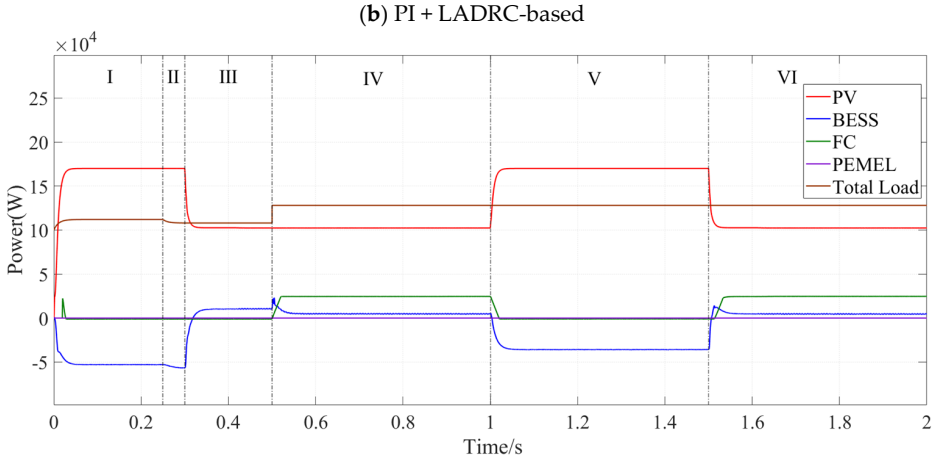

(**c**) PI + PADRC-based

Figure 11. Power dynamics of microgrid components in Scenario I using the three control schemes: (**a**) PI + PI; (**b**) PI + LADRC; (**c**) PI + PADRC.

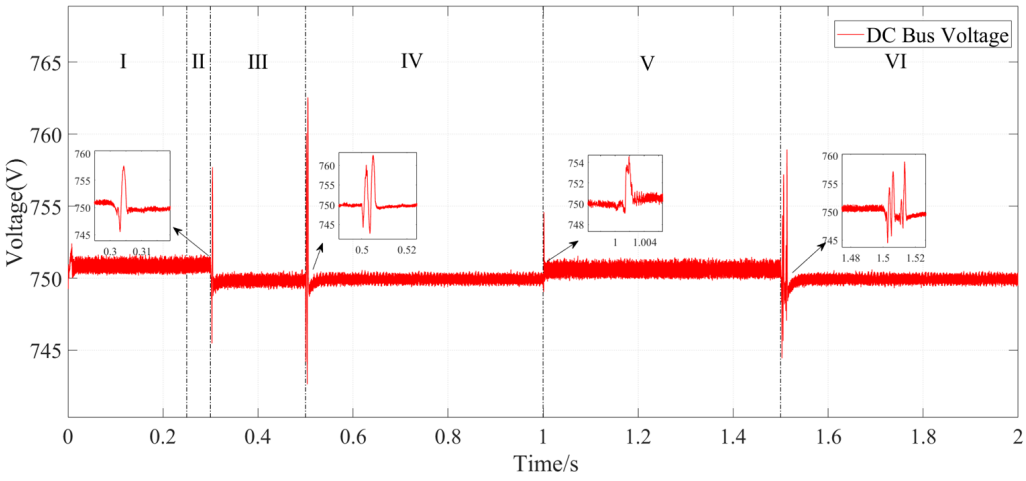

(**a**) PI + PI-based

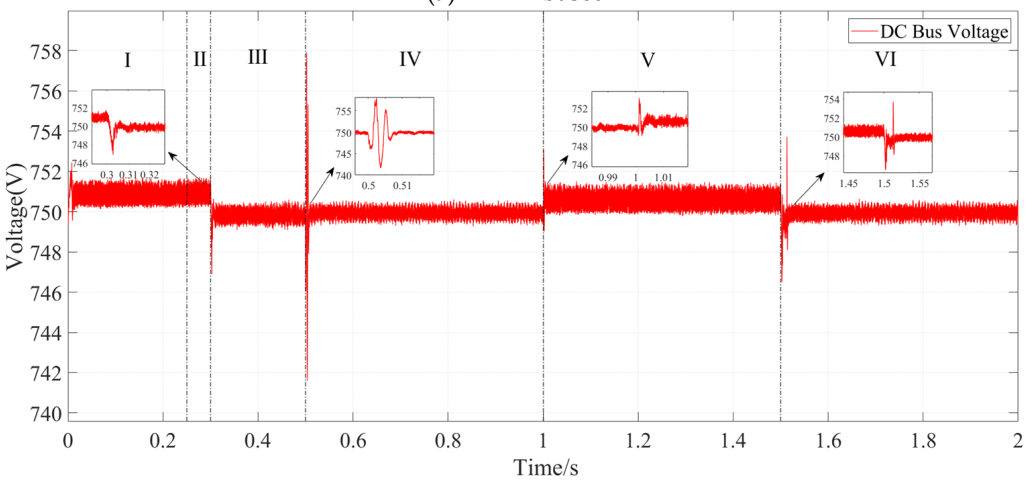

(**b**) PI + LADRC-based

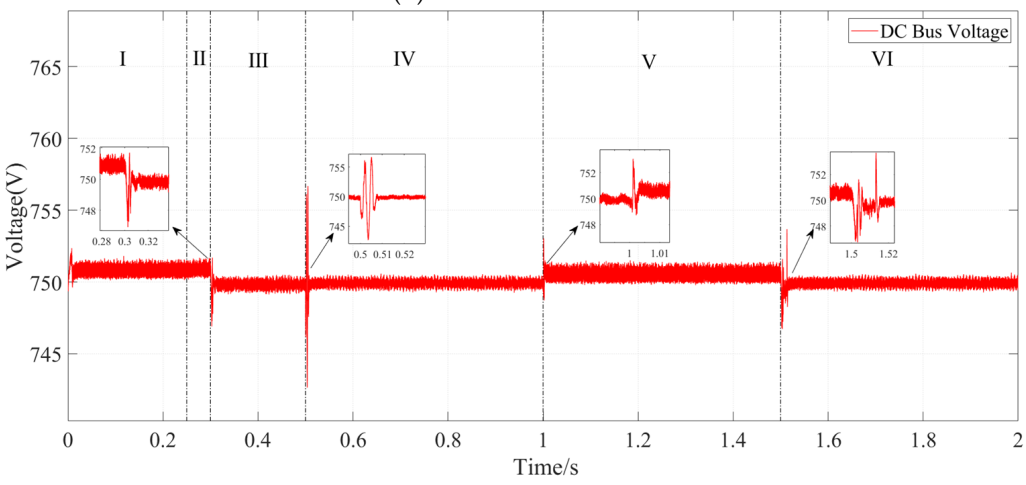

(**c**) PI + PADRC-based

Figure 12. Dynamics of DC bus voltage in Scenario I using the three control schemes: (**a**) PI + PI; (**b**) PI + LADRC; (**c**) PI + PADRC.

During the large disturbance at 0.5 s, the inherent limitations of PI + PI are exposed, with deviations drastically expanding to −7.4 V/+12.6 V. The PI + LADRC reduces the positive deviation to +7.8 V, while the PI + PADRC further restricts the maximum positive deviation to +6.7 V, demonstrating the superior disturbance rejection capability of the proposed PADRC under severe transients.

The inductor current tracking dynamics using the three control schemes in Scenario I are illustrated in Figure 13a–c. For the PI + PI, when the operating condition changes at 0.3 s, the system current reaches steady state at 0.39 s (i.e., a settling time of 0.09 s), achieving accurate reference tracking. When the disturbance occurs at 0.5 s or 1.5 s, the corresponding settling time is 0.08 s or 0.1 s, respectively. Comparatively, using the PI + LADRC and PI + PADRC control schemes, the reference trajectory is nearly replicated with negligible deviations, showing better performance in inductor current tracking than the PI + PI scheme.

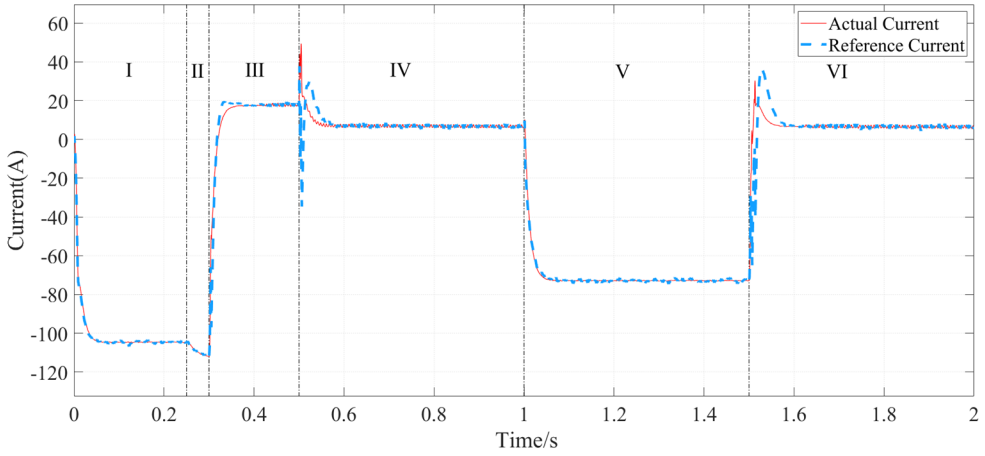

(**a**) PI + PI-based

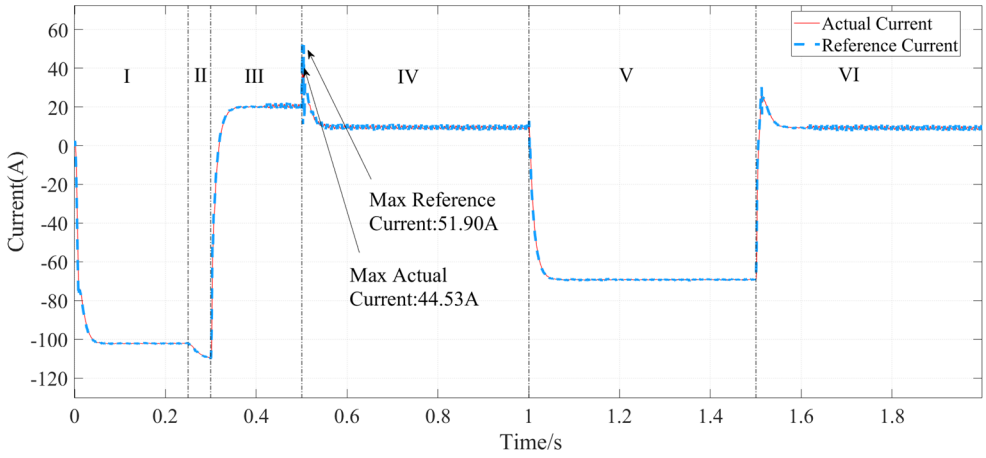

(**b**) PI + LADRC-based

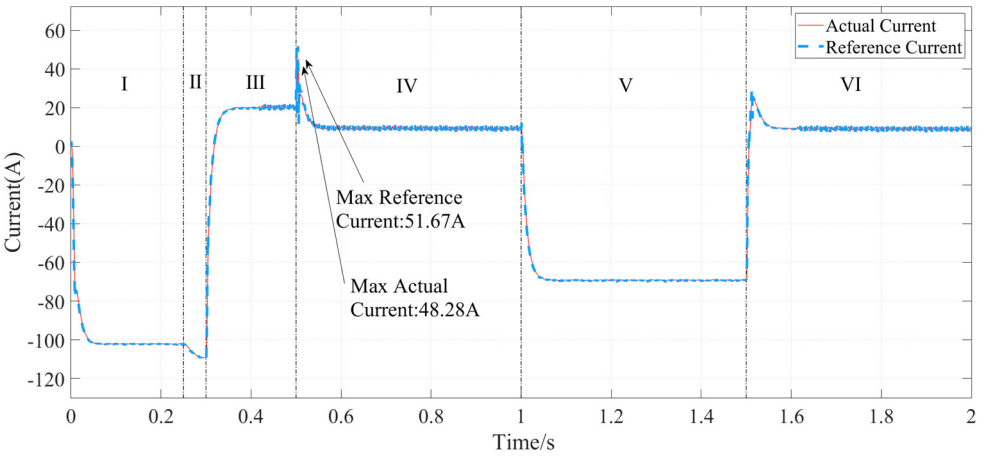

(**c**) PI + PADRC-based

Figure 13. Dynamics of inductor current tracking in Scenario I using the three control schemes: (**a**) PI + PI; (**b**) PI + LADRC; (**c**) PI + PADRC.

It is noted that, given the relatively larger disturbance at 0.5 s, the proposed PI + PADRC (or conventional PI + LADRC) achieves a maximum reference current of 51.67 A (or 51.9 A) and a maximum actual current of 48.28 A (or 44.53 A), respectively. This means that the use of PADRC reduces the inductor current tracking error from 7.37 A to 3.39 A, i.e., results in an improvement of around 54%, due to the adaptive bandwidth expansion and variable damping characteristics of the proposed observer. Collectively, these results illustrate that PI + PADRC achieves faster disturbance estimation, more efficient feedforward compensation, and superior current tracking performance during large disturbances.

4.1.2. Scenario II with High SOC and Low SOHC

Scenario II starts with initial conditions of SOC = 90% and SOHC = 20%, in which case the surplus or shortage of PV power outputs would be consumed by the PEMEL or supplemented by the BESS, respectively. Table 5 lists the designed variations in PV outputs, DC loads, and AC loads over a 2 s interval.

Table 5. Variations of PV outputs, DC loads, and AC loads in Scenario II.

Power \ Time	Stage I 0–0.25 s	Stage II 0.25–0.3 s	Stage III 0.3–0.45 s	Stage IV 0.45–1.5 s	Stage V 1.5–2 s
PV Power (kW)	170	170	102.5	170	170
DC Load (kW)	12	8	8	8	8
AC Load (kW)	100	100	100	100	110

The dynamics of PV outputs, BESS export, FC export, PEMEL loads, and total microgrid loads using the three control schemes in Scenario II are shown in Figure 14a–c. Similar to Scenario I, compared with the PI + PI scheme, the PI + LADRC and PI + PADRC schemes give relatively more stable BESS responses for the disturbance occurring at 0.45 s or 1.5 s.

The corresponding dynamics of DC bus voltage using the three control schemes in Scenario II are shown in Figure 15a–c. Similarly, the events at 0.25 s, 0.3 s, and 0.45 s are classified as small disturbances, while the event at 1.5 s is classified as a large disturbance. Under the small disturbance conditions at 0.3 s and 0.45 s, the PI + PI scheme results in maximum deviations of −3.6 V/+6.1 V and −1.4 V/+1.9 V, as tabulated in Table 6. PI + PADRC effectively tightens these bounds to −3.0 V/+1.9 V and −1.4 V/+1.6 V, respectively. The negligible difference between PI + PADRC and PI + LADRC during these events implies that the threshold mechanism successfully maintains steady-state performance comparable to the linear counterpart.

Under the large disturbance condition at 1.5 s, the PI + PI scheme suffers from severe deviations of −4.5 V/+13.5 V, revealing its limitations during severe transients. PI + LADRC reduces this to −2.4 V/+3.1 V, which is further refined to −2.0 V/+2.8 V by PI + PADRC. This distinct suppression of the positive overshoot stems from the adaptive bandwidth expansion and variable damping characteristics of the proposed observer.

The inductor current tracking dynamics using the three control schemes in Scenario II are shown in Figure 16a–c. The PI + PI scheme manages to reach steady state within 0.08 s after the disturbance occurrence at 0.3 s. This is evidenced by the settling duration of 0.056 s after the disturbance at 0.45 s and a notably sluggish settling time of 0.079 s after the disturbance at 1.5 s. In stark contrast, both PI + LADRC and PI + PADRC maintain rapid and nearly error-free reference tracking regardless of the disturbance severity.

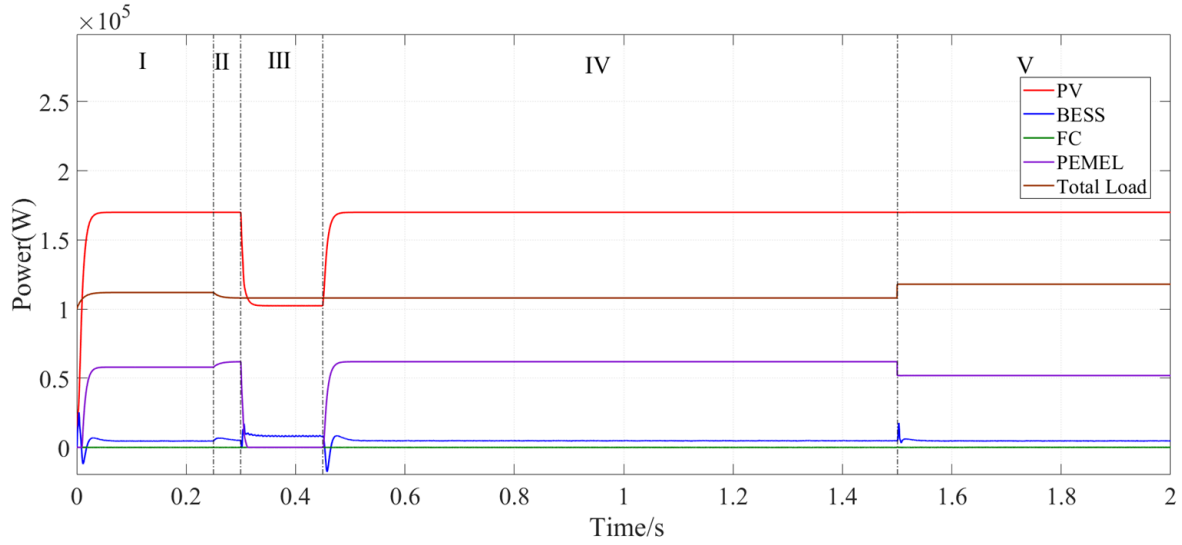

(**a**) PI + PI-based

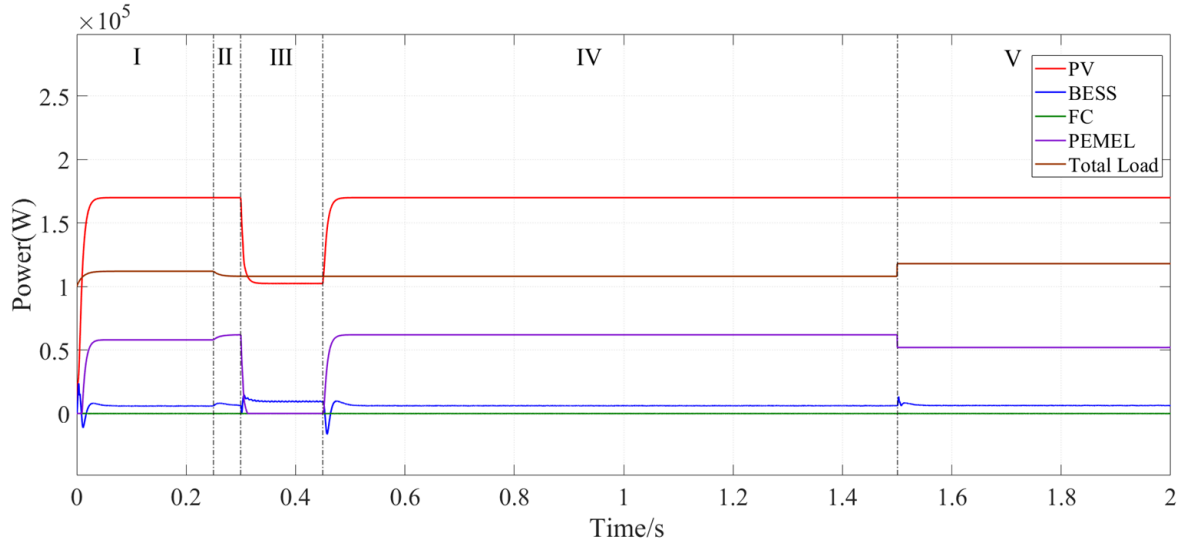

(**b**) PI + LADRC-based

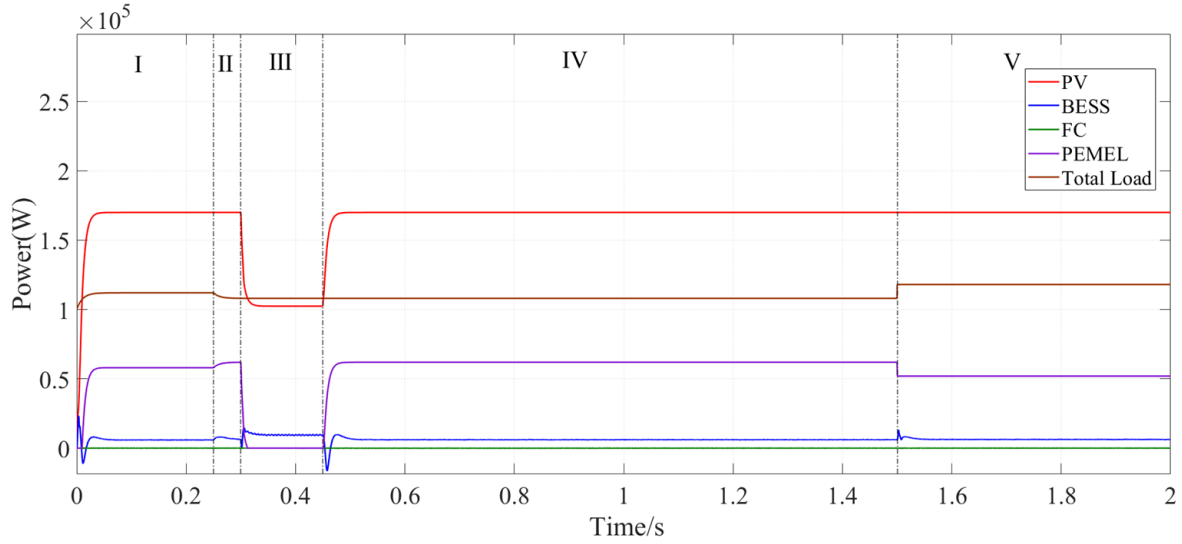

(**c**) PI + PADRC-based

Figure 14. Power dynamics of microgrid components in Scenario II using the three control schemes: (**a**) PI + PI; (**b**) PI + LADRC; (**c**) PI + PADRC.

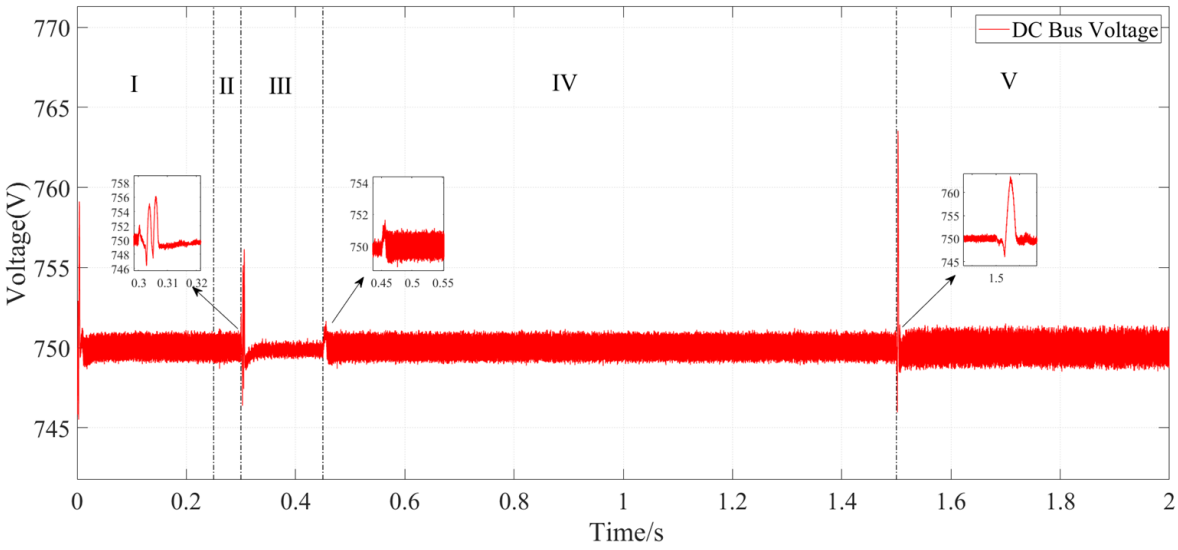

(**a**) PI + PI-based

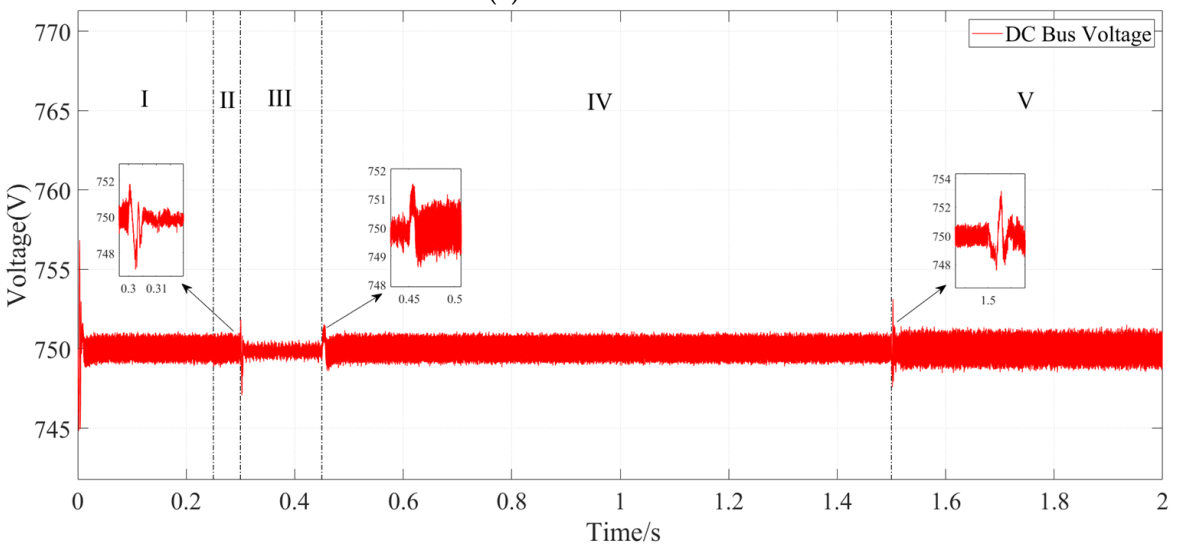

(**b**) PI + LADRC-based

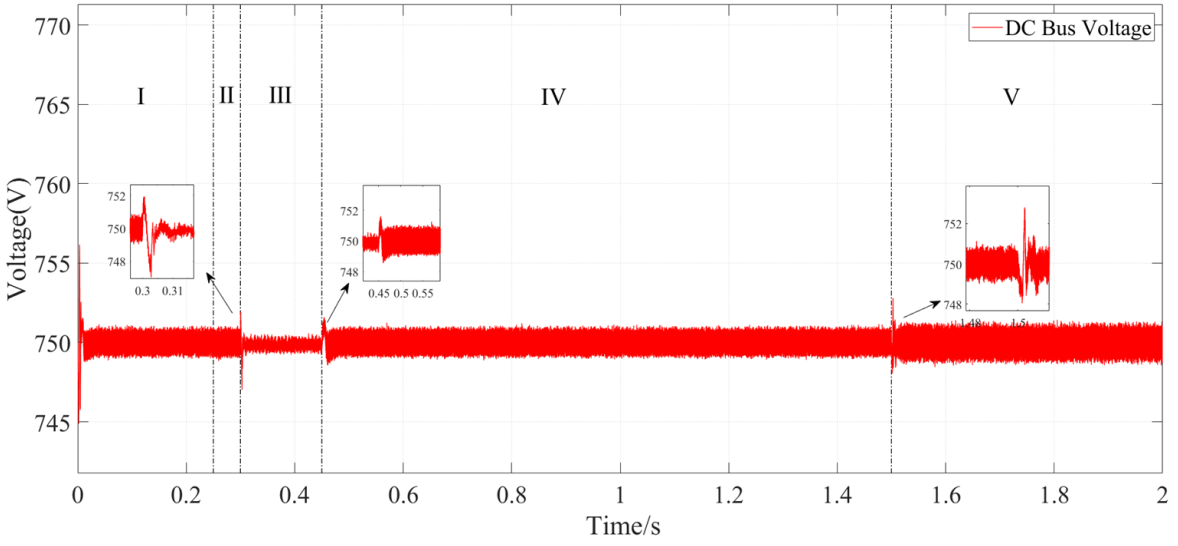

(**c**) PI + PADRC-based

Figure 15. Dynamics of DC bus voltage in Scenario II using the three control schemes: (**a**) PI + PI; (**b**) PI + LADRC; (**c**) PI + PADRC.

Table 6. DC bus voltage fluctuation ranges in Scenario II using the three control schemes.

Disturbance Time (s)	Control Scheme	Bus Voltage Fluctuation Range (V)
0.3	PI + PI	746.4~756.1
	PI + LADRC	747~751.8
	PI + PADRC	747~751.9
0.45	PI + PI	748.6~751.9
	PI + LADRC	748.6~751.5
	PI + PADRC	748.6–751.6
1.5	PI + PI	745.5~763.5
	PI + LADRC	747.6~753.1
	PI + PADRC	748~752.8

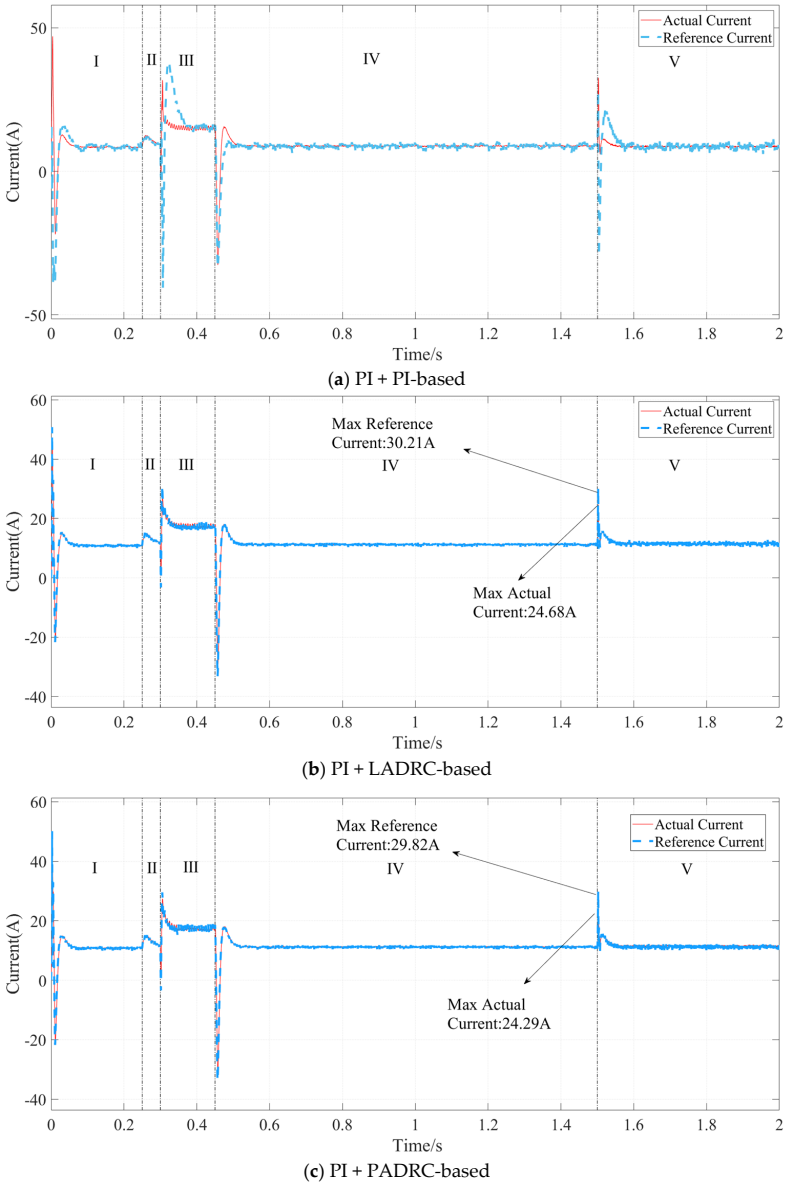

Figure 16. Dynamics of inductor current tracking in Scenario II using the three control schemes: (**a**) PI + PI; (**b**) PI + LADRC; (**c**) PI + PADRC.

A closer examination of the large disturbance event at 1.5 s clarifies the specificity of the proposed method. The maximum absolute error (MAE) is approximately 5.53 A for both PI + LADRC and PI + PADRC, indicating similar initial overshoot magnitudes. However,

the root mean square error (RMSE) of PADRC is 4.13, while that of LADRC is 4.94, which reflects the improvement in control precision that more effectively suppresses disturbances and reduces tracking errors. The distinct MAEs of PADRC in the two scenarios stem from the different system inertias dictated by the initial SOC levels. In Scenario I with low SOC, the aggressive current reference causes severe observation lags in LADRC; thus, PADRC primarily utilises its adaptive bandwidth expansion to reduce tracking errors. Conversely, in Scenario II with high SOC, the current reference after disturbance is more moderate, allowing PADRC to shift its advantage from error reduction to overshoot currents via its enhanced variable damping characteristic.

Comprehensive comparison between Scenarios I and II reveals significant differences in dynamic voltage suppression capabilities. During small disturbances, PI + PADRC and PI + LADRC exhibit nearly identical performance, consistently restricting maximum deviations to within ±4 V and effectively eliminating the severe overshoots (up to +8.9 V) seen in PI + PI. However, during large disturbances, the distinction between the two ADRC-based schemes becomes evident. While PI + PI suffers from extreme deviations exceeding +10 V, PI + LADRC manages to contain the fluctuations, yet PI + PADRC further tightens these bounds. This distinct advantage of PI + PADRC during severe transients stems from its activated nonlinear terms, which provide adaptive bandwidth expansion and variable damping to suppress the residual overshoots that LADRC fails to eliminate.

4.2. Fault-Resilient Control Switching

To verify the effectiveness of the proposed fault-resilient control switching of the FC as a backup power supply to AC loads in converter fault events, Scenario III is designed to start with initial conditions of SOC = 50% and SOHC = 50% (representing a typical operating condition) and experience an AC–DC converter fault at 0.2 s. The dynamics of component power outputs, SOC and SOHC, DC bus voltage, AC bus voltage, and frequencies are shown in Figure 17a–e, respectively.

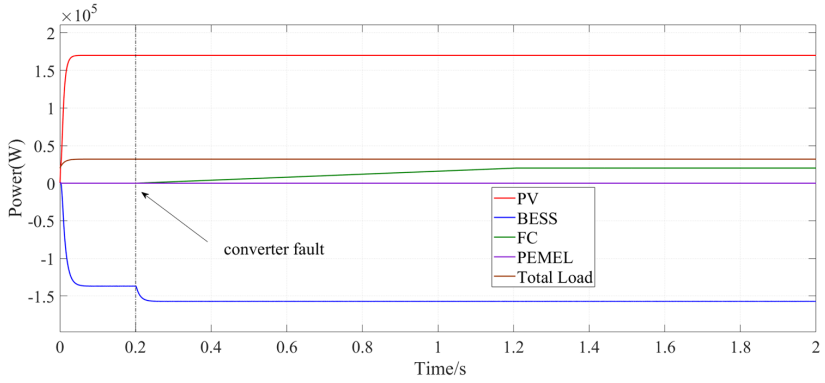

(**a**) Power dynamics

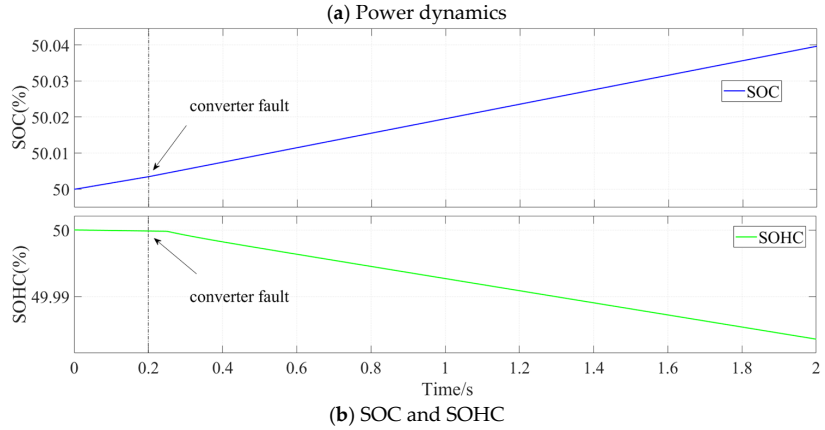

(**b**) SOC and SOHC

Figure 17. *Cont.*

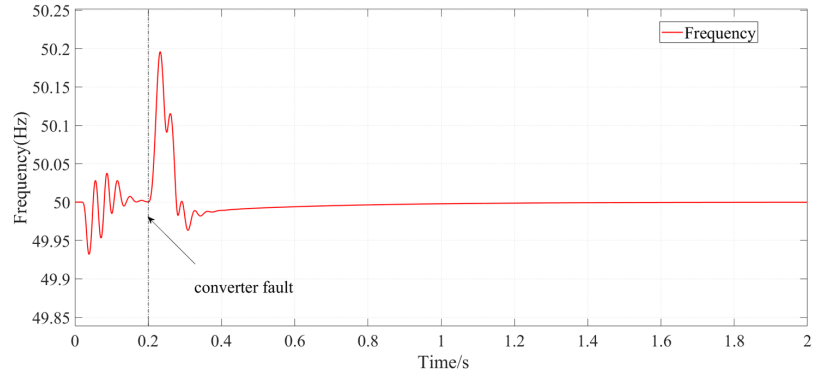

(**c**) AC-side frequency

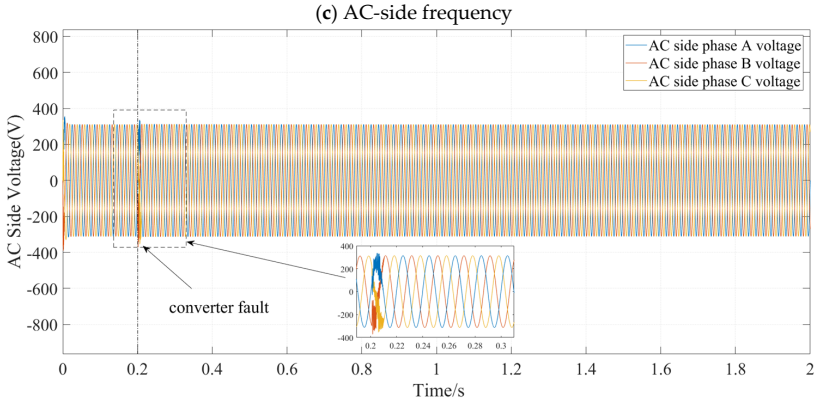

(**d**) Three-phase voltage on AC side

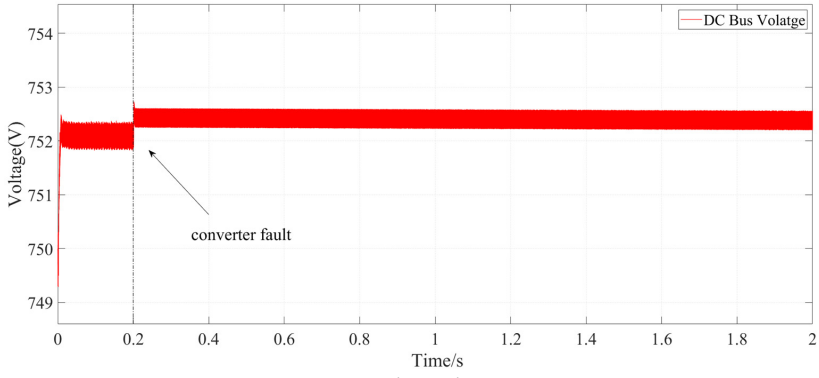

(**e**) DC bus voltage

Figure 17. System dynamics in Scenario III with a DC–AC converter fault occurrence at 0.2 s: (**a**) power dynamics; (**b**) SOC of the BESS and SOHC of the hydrogen storage tank; (**c**) AC-side frequency; (**d**) AC-side voltage; and (**e**) DC bus voltage.

Once the converter DC input voltage drops to zero, a detection persistence time of 1 ms is incorporated into the detection logic to serve as hysteresis, effectively suppressing false triggers caused by transient voltage spikes. Only when the zero-voltage condition persists beyond this 1 ms threshold is the RS latch set and the fault confirmed. After this delay, the control mode of the FC is switched from P-Q to V-f. However, due to the aforementioned physical constraint from the air compressor, the FC power output does not exhibit a sudden 20 kW step jump; instead, it rises gradually at the pre-set 20 kW/s slope. As designed, the initialisation of control and modulation states—specifically the alignment of the V-f controller's pre-fault voltage, frequency, and integrator states and the synchronisation of the SPWM carrier phase—successfully prevents abrupt changes in the AC voltage and frequency reference. The resulting time of 21.654 ms represents the total response time encompassing the detection delay, fault isolation by the RS latch, and the convergence of the newly initialised V-f control loops, as shown in Figure 17a. Simultaneously, the DC side transitions to independently operate as a PV–BESS–load

system, maintaining power supply to the DC load as well. Following the fault, the SOHC of the hydrogen storage tank begins to decrease steadily as the FC consumes hydrogen to sustain AC loads, while the SOC of the BESS steadily increases due to it absorbing the exceedance of PV power outputs over DC loads, as shown in Figure 17b. There is a minor transient fluctuation in the system frequency due to the sudden loss of the master converter. However, employing the virtual inertia provided by the V-f control of the FC, the AC frequency rapidly recovers and stabilises at the nominal 50 Hz, as shown in Figure 17c. Specifically, the frequency is bounded between a peak of 50.19 Hz and a valley of 49.97 Hz. Following the occurrence of the DC–AC converter, both the DC and AC bus voltages successfully return to and maintain stable operation, without experiencing out-of-limit conditions, as shown in Figures 17d and 17e, respectively. Quantitatively, the DC bus voltage exhibits a maximum overshoot of only 2.7 V, while the AC voltage maximum deviation is limited to 21.8 V. Furthermore, the total harmonic distortion (THD) of the AC voltage is maintained at 2.45%, which is well within the acceptable limits for microgrid power quality [34]. These confirm that the BESS and the FC successfully perform their grid-forming roles on the DC and AC sides, respectively, ensuring the voltage (and also frequency for AC) stability of the decoupled DC and AC systems. Collectively, these results verify that the proposed fault-resilient control via the synergy of FC and the BESS effectively guarantees the survivability and operational continuity of the electric–hydrogen AC–DC hybrid microgrid in converter fault scenarios. Notably, in the event of a severe converter fault, the rule-based power distribution strategy becomes partially compromised. When PV generation exceeds the load demand, power allocation to the PEMEL for absorption still adheres to the energy management strategies. Conversely, when PV generation is less than the load demand, power distribution is directly adjusted based on topology variations, with the FC exclusively supplying the AC load and the battery balancing the DC-side power. It is acknowledged that, under more extreme conditions—e.g., AC load transients beyond the fuel cell's physical ramp capability or critically low hydrogen storage—the system would require additional load-shedding measures.

It should be noted that the FC model adopted in this study is a quasi-static representation that captures the steady-state voltage current characteristics but does not incorporate the detailed electro-\chemical dynamics such as gas transport, compressor inertia, and water management. The multi-physics transient behaviour, including reactant starvation and the role of auxiliary energy storage, is beyond the scope of this work and will be addressed in future studies.

5. Conclusions

This paper has investigated a fault-resilient coordinated voltage control method for an islanded AC–DC electric–hydrogen hybrid microgrid. A key contribution was the development of a unified cooperative control scheme that synergistically integrated dynamic voltage stabilisation with fault-tolerant operation. The proposed scheme has successfully mitigated DC bus voltage fluctuations induced by renewable intermittency and frequent load switching, while substantially enhancing system resilience under converter faults.

To address DC bus voltage fluctuations, a hybrid voltage stabilisation control scheme combining an outer-loop PI controller with an inner-loop PADRC was proposed for the bidirectional DC–DC converter. Comparative simulations demonstrated that, during small disturbances, both PI + LADRC and PI + PADRC reduce DC bus voltage fluctuations compared to conventional PI + PI, with negligible differences between them. However, during large disturbances, PI + PADRC consistently achieved the smallest voltage fluctuation, outperforming PI + LADRC by about 14% due to its adaptive bandwidth expansion and variable damping characteristics. Furthermore, the BESS exhibits significantly smoother

transient responses with PI + PADRC, effectively mitigating the risk of overcharge and over-discharge. Consequently, the PI + PADRC control scheme demonstrated superior overall performance, particularly in handling severe transients.

To overcome the inherent vulnerability of islanded microgrids to severe complete disconnection converter faults that decoupled the DC and AC sides, a multi-mode state-switching control mechanism triggered by real-time fault detection has been designed. Upon detecting a fault in the converter's DC input voltage, the fuel cell system rapidly and seamlessly transitions from a standard grid-following (PQ) control mode to an islanded grid-forming (V-f) control mode, concurrently acting as a backup unit to sustain AC loads. By directly inheriting the pre-fault voltage and frequency on AC side as initial control parameters, this mechanism effectively avoids transient shocks to the loads. The proposed fault-resilient control scheme has guaranteed continuous and reliable power supply to critical AC and DC loads through the synergy of batteries and fuel cells, thereby ensuring the survivability and operational continuity of the microgrid under extreme fault scenarios.

Building on the microgrid model and control schemes developed in this work, semi-physical simulation experiments will be conducted using a real-time simulation platform to evaluate model and control performance under complex environments. Crucially, leveraging the capabilities of real-time platforms, the simulation window will be significantly extended from the current second-level scale to minute or hour scales. This long-term evaluation will effectively illustrate the gradual evolution of the SOC and SOHC. Furthermore, future work will implement field tests based on the real-world electric–hydrogen hybrid microgrid to validate the effectiveness of the proposed control method in practice. Finally, since the current study utilises a static FC model to focus on millisecond-level voltage transients, future work will aim to integrate this fault-resilient control framework with dynamic state of health estimation and lifespan prediction for FCs, thereby ensuring the long-term operational robustness of the microgrid.

Supplementary Materials: The following supporting information can be downloaded at: https://www.mdpi.com/article/10.3390/electronics15174021/s1, Figure S1. Simulation modules of PV panels within microgrid. Figure S2. Simulation modules of BESS within microgrid. Figure S3. Simulation modules of electrolyser and hydrogen storage tank within microgrid. Figure S4. Simulation modules of VSG control of master converter. Figure S5. Power dynamics of microgrid components in Scenario I under the PI+FCS-MPC. Figure S6. Dynamics of DC bus voltage in Scenario I under the PI+FCS-MPC. Table S1. DC bus voltage fluctuation ranges in Scenario I under the PI+FCS-MPC. Figure S7. Dynamics of inductor current tracking in Scenario I under the PI+FCS-MPC. Figure S8. Power dynamics of microgrid components in Scenario II under the PI+FCS-MPC. Figure S9. Dynamics of DC bus voltage in Scenario II under the PI+FCS-MPC. Table S2. DC bus voltage fluctuation ranges in Scenario II under the PI+FCS-MPC. Figure S10. Dynamics of inductor current tracking in Scenario II under the PI+FCS-MPC. Figure S11. Power dynamics of microgrid components with noise injection into the inductive loop in Scenario I.

Author Contributions: Conceptualisation, K.S. and Z.C.; methodology, H.Y., Z.W., S.Z., and F.F.; software, H.Y. and Z.W.; validation, H.Y., Z.W., S.Z., F.F., and J.Z.; formal analysis, H.Y., Z.W., S.Z., F.F., and J.Z.; investigation, H.Y., Z.W., S.Z., F.F., and J.Z.; resources, K.S. and Z.C.; data curation, H.Y. and J.Z.; writing—original draft preparation, H.Y. and F.F.; writing—review and editing, K.S. and J.Z.; visualisation, H.Y.; supervision, F.F. and K.S.; project administration, K.S. and Z.C.; funding acquisition, K.S. and Z.C. All authors have read and agreed to the published version of the manuscript.

Funding: We acknowledge the support of the Shenzhen Energy Group Company Ltd. for the Key Technology Research Project of the Integrated Energy Utilization System of Photovoltaic Green Hydrogen.

Data Availability Statement: The original contributions presented in this study are included in the article. Further inquiries can be directed to the corresponding authors.

Conflicts of Interest: Authors Jingran Zhang and Zhengjian Chen were employed by the Shenzhen Energy Group Company Ltd. The authors declare that this study received funding from Shenzhen Energy Group Company Ltd. The funder was not involved in the study design, the data collection, analysis, or interpretation, the writing of this article, or the decision to submit it for publication. The remaining authors declare that the research was conducted in the absence of any commercial or financial relationships that could be construed as a potential conflict of interest.

References

1. Zhang, Z.G.; Kang, C.Q. Challenges and prospects for constructing the new-type power system towards a carbon neutrality future. *Proc. CSEE* **2022**, *42*, 2806–2819. [CrossRef]
2. Fita, N.D.; Obretenova, M.I.; Marcu, M.D.; Olteanu, C.R.; Popescu, F.G.; Manafu, M.G.; Muresan-Grecu, F.; Schiopu, A.M.; Diodiu, I.L.; Nicola, A.; et al. Risk Management of Microgrids in Power System for Enhanced Energy Security and National Resilience. *Electronics* **2026**, *15*, 2397. [CrossRef]
3. Wang, C.S.; Wu, Z.; Li, P. Research on key technologies of microgrid. *Trans. China Electrotech. Soc.* **2014**, *29*, TM732. [CrossRef]
4. Li, J.; Shi, Z.; Liang, Z. A Review on Electricity-Hydrogen Coupling System: Methodologies, Applications, and Prospects. *J. Mod. Power Syst. Clean Energy* **2026**, *14*, 399–415. [CrossRef]
5. Yue, M.; Lambert, H.; Pahon, E.; Roche, R.; Jemei, S.; Hissel, D. Hydrogen energy systems: A critical review of technologies, applications, trends and challenges. *Renew. Sustain. Energy Rev.* **2021**, *146*, 111180. [CrossRef]
6. Jiang, L.; Fu, X. An Ammonia–Hydrogen Energy Roadmap for Carbon Neutrality: Opportunity and Challenges in China. *Engineering* **2021**, *7*, 1688–1691. [CrossRef]
7. Huang, Y.; Huang, W.; Lin, L.; Cao, Y.; Luo, Y.; Lin, X.; Jiang, L. Design of a Radial Flow Fixed-Bed Reactor with Integrated Variable Heat Exchange for More Efficient and Purer Hydrogen Production via Water Gas Shift Reaction. *Int. J. Hydrogen Energy* **2025**, *99*, 685–696. [CrossRef]
8. Zhu, X.R.; Xie, Z.Y.; Jing, S.Z. Virtual inertia control and stability analysis of DC micro-grid. *Power Syst. Technol.* **2017**, *41*, 3884–3893. [CrossRef]
9. Panda, S.; Biswal, G.R.; Subudhi, B. Enhancing Voltage Regulation in Standalone Microgrid Using a Model Reference Adaptive Control Approach. In Proceedings of the International Conference on Electric Power and Renewable Energy (EPREC), NIT, Jamshedpur, India, 24–26 May 2024; pp. 53–67. [CrossRef]
10. Kanniappen, S.M.; Pillay, N.; Lazarus, I.J. Bus Voltage Regulation of a DC Microgrid using Cascade PID Control. In Proceedings of the 2025 Conference on Information Communications Technology and Society (ICTAS), Durban, South Africa, 23–25 July 2025; pp. 1–6. [CrossRef]
11. Mesbah, M.A.; Sayed, K.; Ahmed, A.; Aref, M.; Elbarbary, Z.M.S.; Almuflih, A.S.; Mossa, M.A. Adaptive Control Approach for Accurate Current Sharing and Voltage Regulation in DC Microgrid Applications. *Energies* **2024**, *17*, 284. [CrossRef]
12. Thambi, S.; R, B.K.; P, K. Piece-wise Droop Control Algorithm in Renewable Fed DC Microgrid Voltage Regulation using Super-capacitors. *Smart Grids Sustain. Energy* **2024**, *9*, 26. [CrossRef]
13. Liu, S.; Zheng, J.; Li, Z.; Li, R.; Fang, W.; Liu, X. Distributed Piecewise Droop Control of DC Microgrid with Improved Load Sharing and Voltage Compensation. In Proceedings of the 2019 IEEE Third International Conference on DC Microgrids (ICDCM), Matsue, Japan, 20–23 May 2019; pp. 1–6. [CrossRef]
14. Tao, L.; Liu, Y.; Zhou, X.; Lian, J.; Wen, H. Adaptive ADRC Method with Dual-Loop Gain for Microgrid Voltage Control in the Offshore Energy Island. *Electr. Power Syst. Res.* **2026**, *258*, 113127. [CrossRef]
15. Saha, S.; Gholami, S.; Khan, P.M.K. Sensor Fault-Resilient Control of Electronically Coupled Distributed Energy Resources in Islanded Microgrids. *IEEE Trans. Ind. Appl.* **2022**, *58*, 914–929. [CrossRef]
16. Feng, Y.; Xu, X. Actuator and Sensor Faults Resilient Control Strategy of Microgrids. In Proceedings of the 2025 37th Chinese Control and Decision Conference (CCDC), Xiamen, China, 16–19 May 2025; pp. 5872–5879. [CrossRef]
17. Jadidi, S.; Badihi, H.; Zhang, Y. Active Fault-Tolerant and Attack-Resilient Control for a Renewable Microgrid Against Power-Loss Faults and Data Integrity Attacks. *IEEE Trans. Cybern.* **2024**, *54*, 2113–2128. [CrossRef] [PubMed]
18. Jagadeesh, P.; Siva, A.; Mounica, P.; Ahmed, M.A. Advanced control strategy for a wind-hydrogen-battery standalone microgrid under distribution line fault conditions. *Int. J. Powertrains* **2025**, *14*, 264–276. [CrossRef]
19. Xiao, X. Basic problems of the new complex AC-DC power grid with multiple energy resources and multiple conversions. *Trans. China Electrotech. Soc.* **2015**, *30*, TM721. [CrossRef]
20. Manna, S.; Singh, D.K.; Akella, A.K.; Kotb, H.; AboRas, K.M.; Zawbaa, H.M.; Kamel, S. Design and implementation of a new adaptive MPPT controller for solar PV systems. *Energy Rep.* **2023**, *9*, 1818–1829. [CrossRef]

21. Su, Y.; Peng, F.; Li, G.; Liu, H.; Zhong, Y.; Yuan, Y.; Wang, D.; Xie, H. Modeling and Stability Analysis of a PV–Energy Storage AC/DC Integrated Three-Port Grid-Connected Power Electronic Device. *Electronics* **2026**, *15*, 3411. [CrossRef]
22. Wang, C.; Jiao, S.; Zhang, Y.; Wang, X.; Li, Y. Adaptive Variable Universe Fuzzy Droop Control Based on a Novel Multi-Strategy Harris Hawk Optimization Algorithm for a Direct Current Microgrid with Hybrid Energy Storage. *Energies* **2024**, *17*, 5296. [CrossRef]
23. Yan, K.; Long, X.; Lu, J.; Liu, Y.; Wu, Y. Simplified Mechanism Modeling and Discharge Characteristic Analysis of High-Rate LiFePO4 Batteries. *Trans. China Electrotech. Soc.* **2022**, *37*, 599–609. [CrossRef]
24. Khayrullina, A.G.; Blinov, D.; Borzenko, V. Novel kW scale hydrogen energy storage system utilizing fuel cell exhaust air for hydrogen desorption process from metal hydride reactor. *Energy* **2019**, *183*, 1244–1252. [CrossRef]
25. Dash, V.; Bajpai, P. Power management control strategy for a stand-alone solar photovoltaic-fuel cell–battery hybrid system. *Sustain. Energy Technol. Assess.* **2015**, *9*, 68–80. [CrossRef]
26. Al-Mandhari, M.; Ghosh, A. Modelling Solar Intermittency Effects on PEM Electrolyser Performance & Degradation: A Comparison of Oman and UK. *Energies* **2025**, *18*, 6131. [CrossRef]
27. Li, J.; Shi, Z.; Qiao, Y.; Jiang, X. Optimal Configuration of Hydrogen Energy Storage Systems Considering the Operational Efficiency Characteristics of Multi-Stack Electrolyzers. *Modelling* **2025**, *6*, 101. [CrossRef]
28. Wang, Z.; Fan, F.; Zhang, H.; Song, K.; Jiang, J.; Sun, C.; Xue, R.; Zhang, J.; Chen, Z. Flexible On-Grid and Off-Grid Control for Electric–Hydrogen Coupling Microgrids. *Energies* **2025**, *18*, 985. [CrossRef]
29. Wang, L.; Zhou, F.; Nie, P.; Hashimoto, S.; Kawaguchi, T. Dual-Layer Multi-Port High-Gain DC-DC Power Converter with Hybrid Voltage/Current Distribution Strategy. *Electronics* **2026**, *15*, 1454. [CrossRef]
30. Liu, K.; Zhang, L.; Kang, W. Research on Linear Active Disturbance Rejection Control Based on Grid-Forming Distributed Photovoltaics. *Electronics* **2024**, *13*, 3017. [CrossRef]
31. Li, H.; Liu, X.; Lu, J. Research on Linear Active Disturbance Rejection Control in DC/DC Boost Converter. *Electronics* **2019**, *8*, 1249. [CrossRef]
32. Ma, R.; Cheng, Y.; Wang, S.; Sun, S.; Cong, W. Generalized Dynamic Security Region of Grid-Following and Grid-Forming Converter-Based Systems by Basin of Attraction Method. *Appl. Sci.* **2026**, *16*, 2130. [CrossRef]
33. Zhang, H.; Fan, F.; Song, K.; Jiang, J.; Sun, C.; Xue, R. Capacity allocation of hydrogen energy microgrid considering dynamic security constraints of electrolyzers. *Autom. Electr. Power Syst.* **2026**, *50*, 53–62. [CrossRef]
34. Smail, A.A.A.; Mbungu, N.T.; Elnady, A.; Bansal, R.C.; Abo-Khalil, A.G.; Hamid, A.-K.; Bashir, S.B.; Joy, E.R.; Obaid Alyammahi, A.K.S. Master-slave control schemes for microgrids: A critical review. *Renew. Sustain. Energy Rev.* **2026**, *238*, 117065. [CrossRef]

Disclaimer/Publisher's Note: The statements, opinions and data contained in all publications are solely those of the individual author(s) and contributor(s) and not of MDPI and/or the editor(s). MDPI and/or the editor(s) disclaim responsibility for any injury to people or property resulting from any ideas, methods, instructions or products referred to in the content.